

# POLYTECHNIC OF TURIN

Automotive Engineering



Master Degree Thesis

## EFFECT OF THE TIRES POSITION WITH RESPECT TO THE TIRE-BELTS ON AERODYNAMIC COEFFICIENTS

Supervisors

Prof. Andrea TONOLI

Ing. Matteo GAUTERO

Candidate

Luigi CIMIERI

Academic Year's 2022/2023

# Summary

The aim of this thesis is to shift the focus towards the precise positioning of the wheels concerning the rotational airflow within a wind tunnel. Earlier studies and research have revealed the significant influence that wheel positioning exerts on both aerodynamic coefficients and emissions.

To investigate this impact, two distinct methodologies will be employed to set up the most robust correlation between real-world observations and virtual simulations. In today's computing landscape, the available resources enable automotive companies to achieve a strong correlation between numerical Computational Fluid Dynamics (CFD) simulations and wind tunnel experiments. CFD simulations, in comparison to wind tunnel tests, offer cost-effectiveness and flexibility, allowing the examination of different models without the need for constant prototype changes, along with the exploration of various flow field attributes. However, certain scenarios, such as simulating rotating wheels, continue to be areas where the correlation with wind tunnel tests still is under scrutiny. In the first chapters of this thesis, a comprehensive overview of fluid dynamics concepts will be provided, with particular emphasis on the Navier-Stokes equations and turbulence models, including their relevance to the study at hand. Subsequently, concepts of vehicle aerodynamics will be introduced, with a primary focus on airflow around tires. Following this, the fundamentals of computational fluid dynamics will be delved into, detailing its tools and methodologies, while preparing the ground for the experimental analysis.

The experimental part of this research was conducted at the Wind Tunnel of CRF (Centro Ricerche Fiat), a subsidiary of Stellantis, found in Orbassano (TO). The commercial software STAR-CCM+® will be used for numerical simulations, and ANSA for pre-processing operations. ANSA is an advanced multidisciplinary CAE pre-processing tool that offers comprehensive functionality, easing the transition from CAD data to solver-ready input files within a unified environment. In the concluding chapters, the results derived from both methodologies will be presented, aiming to have a discussion regarding the correlation of the discovered aerodynamic coefficients, leading to a conclusion of the work.

# Acknowledgements

I would like to express my heartfelt gratitude to Professor Tonoli, Scantamburlo, and the supervisors of this thesis: Matteo Gautero and Luca Miretti. I am grateful for the knowledge they have imparted in their field, but also for giving me the opportunity to undergo this wonderful experience. Thanks also to Nicola Paola and Francesco Pitillo for their support and endurance during this fantastic journey. Without them, this work would never have come into existence.

Dear mom and dad, in this special moment, I want to dedicate all of this to you, the pillars of my life, for your immense love, unwavering support, and constant inspiration that you have poured onto me. Your commitment, patience, and understanding have created a safe haven where I could grow and learn. This thesis, with every page, is a tribute to your tireless love and infinite dedication.

Dear grandparents, in this moment of joy and achievement, I want to extend a heartfelt thank you to you, the extraordinary people who have shaped my life and academic journey. Your wisdom, unconditional love, and eternal patience have been a constant source of inspiration for me. Every word of wisdom you shared and every affectionate hug contributed to building the foundation of my success. Your presence, even in the most difficult moments, has illuminated my path, providing me with security and affection. This thesis, with all its significance, is a tribute to your love, dedication, and eternal kindness. Thank you from the bottom of my heart for being the extraordinary guides that you are, for making my journey even more special. Thanks to my grandfather Valerio, who has always spoiled, defended, and supported me. Thanks for the hours spent watching me swim, ride a bike, or have fun at the Valente Lido, and for all the calls to check on me. Thanks to my grandmothers Francesca and Maria, also for spoiling me and emphasizing the importance of family, attachment to one's land, and origins. A warm thought goes to my grandfather Luigi; I am sure he is watching over me from above.

I want to thank my second family in Turin, made up of wonderful people who have been present throughout these university years. I thank Antonietta and

Carlo, true grandparents, for always being there. Thanks to Elena and Franco for making me feel like a member of your family. I owe them all a warm hug for being there for me in difficult times and for sharing beautiful moments of carefree joy.

This victory of mine is also dedicated to my brother Valerio, an important, fundamental, and irreplaceable piece of my life. I am grateful for all the affection he has shown me. This thesis is as much mine as yours because every page tells the story of a shared journey. Thank you for being my ally, my confidant, and my adventure companion. The gratitude I feel for having you in my life goes beyond words.

Thanks to my lifelong friends: Carlo, Thomas, Alfredo, and Antonio. You have been the stronghold of the most memorable adventures, the comfort in difficult times, and the endless source of support and understanding. Your constant presence has made every day brighter, and your affection has enriched my life in ways I will never cease to appreciate.

In these years, we have shared joys and struggles, building indelible memories that I will always carry in my heart. Thank you for being the extraordinary friends you are, for sharing the sweetest victories with me, and for being by my side in the toughest moments. And thanks to everyone who joined this family, making everything even more unique.

I thank my friends in Turin: Calogero, Federico, Nico, Angelo, Giulio, Giusy, Chiara, Ginny, Katia, Irene. Our university journey has been an extraordinary adventure, and your friendship has made every step even more meaningful. The shared laughter, sleepless nights, exultant victories, and mutual consolations in difficult times have become the bricks that make up the indestructible structure of our friendship. Thank you for making every university day an unforgettable adventure. The future holds many challenges and successes for us to face together, and I look forward to sharing them with you.

In this moment of reflection and gratitude, I want to thank you, extraordinary fellow travelers along the path of our undergraduate degree: Gloria, Miriana, Luca, Stefano, and Alex. We have shared laughter, challenges, and moments of growth that will remain engraved in the dearest memories of my university experience. Our undergraduate degree has been a fundamental chapter of our lives, and I am grateful to have shared it with you.

Heartfelt thanks also to all my colleagues in Automotive. We have faced complex challenges, learned together, and created bonds that go beyond university classrooms. We have experienced truly crazy adventures, like the adventure at Mugello,

which I will always carry with me. I am grateful to have had your company on this journey.

Finally, I would like to thank colleagues and friends in Homologation. I am facing an exciting journey characterized by shared laughter, overcome challenges, and personal and professional growth. It is a privilege to share not only projects and meetings but also moments of lightness and joy that have made our work environment truly unique. Thank you for your tireless collaboration, dedication, and passion. Every day spent with you has been a chapter in an extraordinary story. And if all this is possible, it is thanks only to Federica, who believed in me that day in January. Thank you for your trust in me. I am grateful for the opportunity to be part of this extraordinary team.

*“The show must go on”*

# Table of Contents

<b>List of Tables</b>	VII
<b>List of Figures</b>	VIII
<b>1 Introduction</b>	1
1.1 Fluid dynamics . . . . .	3
1.2 Continuity Equations . . . . .	4
1.3 Mass Conservation . . . . .	5
1.4 Momentum Conservation . . . . .	5
1.5 Energy Conservation . . . . .	7
1.6 Navier Stokes Equations . . . . .	7
1.7 Reynolds Number . . . . .	8
<b>2 Vehicle Aerodynamics</b>	9
2.1 Streamlines . . . . .	10
2.2 Velocity Distribution . . . . .	11
2.3 Boundary Layer . . . . .	12
2.4 Flow: Laminar and Turbulent . . . . .	13
2.5 Pressure coefficient . . . . .	14
2.6 Vortex flow . . . . .	16
2.7 Wheel Aerodynamics . . . . .	17
2.8 Forces classification . . . . .	19
<b>3 Computational fluid dynamics</b>	22
3.1 Reynolds Averaged Navier-Stokes Equation . . . . .	22
3.2 Modelling Turbulence . . . . .	24
3.3 K- $\epsilon$ standard method . . . . .	25
3.4 Large Eddy Simulation . . . . .	26
3.5 Detached Eddy Simulation . . . . .	27
3.6 Direct Numerical Simulations . . . . .	28
3.7 Methods comparison . . . . .	29

<b>4</b>	<b>Wind Tunnel</b>	<b>31</b>
4.1	Single belt system . . . . .	33
4.2	Five-belt system . . . . .	34
4.3	Aeroacoustics Gallery in Orbassano . . . . .	35
4.4	Rolling Road Simulation System . . . . .	36
4.5	Use of Mini Belts in Wind Tunnel Testing . . . . .	37
<b>5</b>	<b>CFD Analysis</b>	<b>39</b>
5.1	Mesh Generation . . . . .	39
5.2	Introduction of grooved tires . . . . .	41
5.3	Simulation of the various belt configurations . . . . .	43
5.4	Open FOAM . . . . .	46
5.5	Results . . . . .	47
5.5.1	Convergence of the simulations . . . . .	47
5.5.2	Transversal moving 17" wheels case . . . . .	49
5.5.3	Wheel cover case . . . . .	57
5.6	Field Pressure . . . . .	60
<b>6</b>	<b>CFD and WT comparison</b>	<b>69</b>
6.1	Wind tunnel test . . . . .	69
6.2	Aerodynamic coefficients . . . . .	71
6.2.1	Cx Correlation . . . . .	71
6.2.2	Cz correlation . . . . .	73
6.2.3	Flow field . . . . .	80
6.3	Pressure Field . . . . .	83
6.3.1	Cx correlation . . . . .	83
6.3.2	Cz Correlation . . . . .	84
<b>7</b>	<b>Conclusion</b>	<b>89</b>

# List of Tables

6.1	Delta Cx correlation . . . . .	71
6.2	Dispersion values . . . . .	88

# List of Figures

1.1	Total drag distribution . . . . .	2
1.2	Euler and LanGrange Rapresentation . . . . .	4
1.3	Tangential stress . . . . .	6
2.1	Streamlines in a steady-state flow . . . . .	10
2.2	Attached and Separated flow . . . . .	11
2.3	Velocity Distribution . . . . .	11
2.4	Boundary layer . . . . .	12
2.5	Variation of boundary layer thickness . . . . .	13
2.6	Fluid particles in laminar and turbulent flow . . . . .	14
2.7	pressure distribution along the car . . . . .	15
2.8	Vortex flow on generic car shape . . . . .	16
2.9	Vortices around rotating wheel . . . . .	17
2.10	Pressure distribution on a stationary and rotating wheel . . . . .	18
2.11	Forces acting on a rotating wheel . . . . .	19
2.12	Deformations due to inertial forces . . . . .	20
3.1	Comparison of Simulation Methods . . . . .	30
4.1	Single belt moving ground set-up . . . . .	33
4.2	5-belt moving ground set-up . . . . .	34
4.3	Rotating Platform . . . . .	35
4.4	Platform . . . . .	36
4.5	Mini belt . . . . .	37
5.1	Example of Mesh error: Single and Triple Cons . . . . .	40
5.2	Example of Baffle in Stelvio: Heat Exchanger . . . . .	41
5.3	Slick tire . . . . .	42
5.4	Morphing tire . . . . .	42
5.5	Grooved tire . . . . .	43
5.6	Belts in central position . . . . .	44
5.7	Example of possibble belts configurations: maximum external position . . . . .	45

5.8	Belts configuration on Open Foam . . . . .	46
5.9	Convergence in Cx simulation . . . . .	47
5.10	Convergence in Cz simulation . . . . .	48
5.11	Rear belts in external configurations . . . . .	49
5.12	Rear belts in central configuration . . . . .	50
5.13	Rear belts in internal configurations . . . . .	50
5.14	Average Cx during front moving belts . . . . .	51
5.15	Average Cx during rear moving belts . . . . .	51
5.16	Average Cx during front and rear moving belts . . . . .	52
5.17	Velocity of front tires in Front belts central configuration . . . . .	53
5.18	Velocity of front tires in Front belts internal configuration . . . . .	53
5.19	Average Cz during front moving belts . . . . .	54
5.20	Average Cz during rear moving belts . . . . .	54
5.21	Average Cz during front and rear moving belts . . . . .	55
5.22	Average Cza during front moving belts . . . . .	55
5.23	Average Cza during rear moving belts . . . . .	56
5.24	Average Cza during front and rear moving belts . . . . .	56
5.25	Average Czp during front moving belts . . . . .	56
5.26	Average Czp during rear moving belts . . . . .	57
5.27	Average Czp during front and rear moving belts . . . . .	57
5.28	Average Cx during front moving belts with covered wheels . . . . .	58
5.29	Average Cza during front moving belts with covered wheels . . . . .	58
5.30	Average Czp during front moving belts with covered wheels . . . . .	59
5.31	Average Cx during rear moving belts with covered wheels . . . . .	59
5.32	Average Cza during rear moving belts with covered wheels . . . . .	60
5.33	Average Czp during rear moving belts with covered wheels . . . . .	60
5.34	Coordinates of the points around the belt . . . . .	61
5.35	Coordinates of the points in the back . . . . .	61
5.36	Field pressure of tire and belts . . . . .	62
5.37	Cp back comparisons moving the front belts . . . . .	63
5.38	Cp back coefficients during front moving belts . . . . .	63
5.39	Cp back coefficients during rear moving belts . . . . .	64
5.40	Cp back coefficients during front and rear moving belts . . . . .	64
5.41	Cp back coefficients during front and rear moving belts . . . . .	64
5.42	Field pressure of the front right belts in external configurations . . . . .	65
5.43	Field pressure of the front right belts in central configurations . . . . .	65
5.44	Field pressure of the front right belts in internal configurations . . . . .	66
5.45	Front right average Cp during moving front belts . . . . .	66
5.46	Field pressure of the rear right belts in external configurations . . . . .	67
5.47	Field pressure of the rear right belts in internal configurations . . . . .	67
5.48	Field pressure of the rear right belts in internal configurations . . . . .	67

5.49	Rear right average Cp during moving rear belts . . . . .	68
5.50	Front right average Cp during moving rear belts . . . . .	68
5.51	Rear right average Cp during moving front belts . . . . .	68
6.1	Central position between front wheels and WSU . . . . .	69
6.2	Limit condition between wheel and WSU . . . . .	70
6.3	Position sensors on the rear car . . . . .	70
6.4	Position sensors around the wheel . . . . .	71
6.5	Delta Cx correlation . . . . .	72
6.6	Cx trend comparison - Front Wsu . . . . .	73
6.7	Cx trend comparison - Rear Wsu . . . . .	73
6.8	Cz trend comparison - Front Wsu . . . . .	74
6.9	Cz trend comparison - Rear Wsu . . . . .	74
6.10	Cza trend comparison - Front Wsu . . . . .	75
6.11	Cza trend comparison - Rear Wsu . . . . .	75
6.12	Czp trend comparison - Front Wsu . . . . .	76
6.13	Czp trend comparison - Rear Wsu . . . . .	76
6.14	Comparison CFD and WT Cx average during front moving belts with covered wheels . . . . .	77
6.15	Comparison CFD and WT Cx average during reae moving belts with covered wheels . . . . .	78
6.16	Comparison CFD and WT Cza average during front moving belts with covered wheels . . . . .	78
6.17	Comparison CFD and WT Czp average during front moving belts with covered wheels . . . . .	79
6.18	Comparison CFD and WT Cza average during rear moving belts with covered wheels . . . . .	79
6.19	Comparison CFD and WT Czp average during rear moving belts with covered wheels . . . . .	80
6.20	Flow field - front moving belts . . . . .	81
6.21	Flow field - front moving belts with covered tires . . . . .	81
6.22	Flow field - rear moving belts . . . . .	82
6.23	Flow field - rear moving belts with covered tires . . . . .	82
6.24	Comparison of back pressure during front moving belts . . . . .	83
6.25	Comparison of back pressure during rear moving belts . . . . .	83
6.26	Cp comparison - front moving WSU . . . . .	84
6.27	Cp comparison - rear moving WSU . . . . .	84
6.28	Cp comparison - front moving WSU . . . . .	85
6.29	Cp comparison - rear moving WSU . . . . .	85
6.30	Cp dispersion ext WSU . . . . .	86
6.31	Cp dispersion cent WSU . . . . .	86

6.32 Cp dispersion int WSU . . . . .	87
6.33 Cp dispersion ext WSU . . . . .	87
6.34 Cp dispersion cent WSU . . . . .	87
6.35 Cp dispersion int WSU . . . . .	88

# Chapter 1

## Introduction

Nowadays all the automotive company are always in competition to find the best trade-off between the efficiency and costs. Every day it's a big challenge and to reach the best results ever, each of them must be equipped with sophisticated infrastructures. Stellantis is one of the most important automotive companies in the world with the latest modern infrastructure in terms of software and laboratories.

Contemporary computational resources have paved the way for automobile companies to set up a strong correlation between numerical Computational Fluid Dynamics (CFD) simulations and wind tunnel experiments. In contrast to wind tunnel tests, CFD simulations offer cost-effective advantages. They enable the examination of various vehicle models without the necessity for continuous model prototype modifications and supply the flexibility to investigate diverse flow field characteristics. Nevertheless, certain scenarios, such as simulating the dynamics of rotating wheels, still call for ongoing investigation in terms of their correlation with wind tunnel tests. This study will delve into the implementation of different methodologies within commercial CFD software to address this challenge.

In the exploration the airflow patterns surrounding passenger cars, a specific area of interest lies in the behavior of the flow field around the wheels. This aspect significantly affects brake cooling, underbody airflow, as well as the drag and lift forces exerted on the car body. When we analyze realistic car models, we discover that wheels contribute approximately 30 % to the overall drag, with a notable two-thirds of this drag being generated by the rear wheels. The figure illustrates the distribution of total drag along the passenger car, expressed as a percentage.

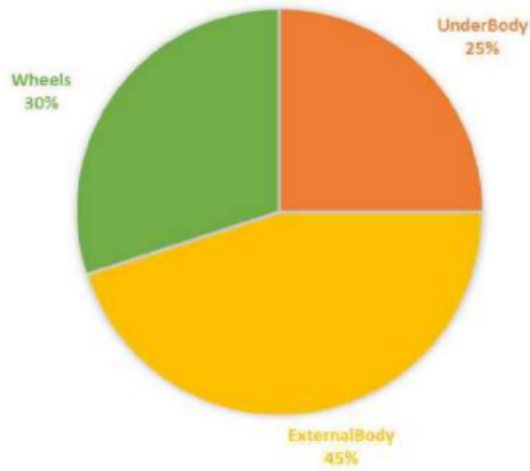


**Figure 1.1:** Total drag distribution

The reason of this study starts from the introduction of a new floor, made of a five- moving belts, which was an upgrade with respect to the earlier wind tunnel, where the whole floor was standing.

The simulation of the moving ground approximate almost the real conditions, but from the aerodynamic POV is important to study the effects around there, due to the physical phenomenon which arise. Especially what we are going to analyze will be how the drag coefficient  $C_x$  changes, changing the position of the wheels with respect to the belts in the three linear directions. All these analyses will be performed both in numerical and experimental way in order to find the correction coefficients which differ the two methods.

## 1.1 Fluid dynamics

A fluid is, in its simplest definition, 'something that flows,' and the study of its motion falls within fluid dynamics. The primitive concept above at once distinguishes fluids from solids, as solids show their own macroscopic shape, and their atoms are more rigidly bonded. Fluids can be essentially classified into two phases: liquid and gas. The main difference between them lies in the intermolecular bonds of the considered materials. The liquid phase is usually found in high-density environments (like on Earth) and is characterized by low compressibility. Gases, on the other hand, are more easily compressible and do not require specific environmental conditions (such as density, temperature, and pressure) to be classified as such.

There is no clear boundary on the possible applications of fluid dynamics in the field of physics and astrophysics. A fluid can be the water in a river or the Earth's atmosphere, for example. To study a specific physical phenomenon using fluid dynamics, the hypothesis of continuity is applied, which involves considering the set of studied objects (atoms, molecules, stars, etc.) as a continuous body. A continuous body is defined as an infinite collection of material points filling an entire regular region of space.

The continuity hypothesis is valid when, for a given physical system, the molecular structure can be neglected. This implies that a small portion of matter (more formally referred to as a volume element) contains a large number of particles; otherwise, the atomic structure cannot be neglected, and the local thermodynamic properties (e.g., pressure, density, temperature, entropy) would not be uniform within the volume element. There are two approaches to formulate the equations of fluid dynamics:

- Eulerian description: This approach studies the variations of physical properties of a small fluid region at a fixed spatial position over time. The physical quantities considered are functions of the position ' $r$ ' of the volume element and time ' $t$ '. The temporal variation of any quantity ' $q$ ' at a fixed position is expressed, in the Eulerian description, as  $\partial q/\partial t$ .
- LaGrange description: In this approach, a particular fluid element is chosen, and its physical properties are studied as they change. In this description, the observer's (spatial) reference frame is fixed to the fluid, and the physical properties depend on the variable position ' $\alpha$ ' of the volume element and time. The LaGrange temporal derivative of a physical quantity ' $q$ ', denoted by  $Dq/Dt$ , is constituted by the partial temporal derivative of ' $q$ ' at a fixed ' $\alpha$ ', which is the Eulerian temporal derivative of ' $q$ ', and the variation of ' $q$ ' in

the new position of the fluid element, as it moves in time with velocity 'v'. In summary, approximating to the first order, it can be written as:

$$\frac{Dq}{Dt} = \frac{\partial q}{\partial t} + \mathbf{v} \cdot \nabla q \quad (1.1)$$



**Figure 1.2:** Euler and Lagrange Representation

$Dq/Dt$  is also referred to as the material derivative, or convective derivative. In conclusion, the Eulerian description pertains to the study of fluids from the perspective of a reference system fixed in time, while the Lagrange description investigates fluid dynamics with a reference system attached to the specific fluid element under consideration. It is noteworthy that the second description is helpful for focusing on the behavior of a particular fluid element. Regardless of whether the first or the second approach is employed for the study, the equations used express the principles of conservation, which form the foundation of physics.

## 1.2 Continuity Equations

The equations of fluid dynamics are based on the conservation laws, already present in Newtonian mechanics. The equations expressing the local conservation of a physical quantity are called continuity equations. There are mainly two methods to derive them. The first approach involves analyzing the fluid from a molecular point of view, considering the fluid composed of a large number of particles whose motion is dictated by the laws of dynamics.

The macroscopic physical phenomenon is then seen because of the microscopic view, and its overall behavior is predicted by the laws of mechanics and probability theory. Assuming the fluid is in equilibrium, this approach yields the continuity equations and the coefficients related to fluid transport, such as the kinematic viscosity. However, this method is incomplete for polyatomic gases and liquids.

The second method is based on deriving the fluid flow equations using the assumption of continuum. In each volume element, which under the earlier assumptions

can be considered as a point in the continuum, the field variables (velocity, pressure, density, etc.) assume a unique value. These variables are governed by a system of differential equations originating from the continuity equations of mass, momentum, and energy. Solving this system expresses the dependence of the field variables on space and time.

By applying the assumption of continuum to the fluid, the continuity equations can be proven through the Reynolds transport theorem, which allows transitioning from the LaGrange coordinate system to the Eulerian coordinate system within a given volume region. Defining  $\alpha$  as a property of the fluid dependent on time, since the volume region moves with the fluid, its integrated temporal variation over the considered volume can be expressed as:

$$\frac{D}{Dt} \int \alpha dV = \int \left( \frac{\partial \alpha}{\partial t} + \nabla \cdot (\alpha \mathbf{v}) \right) dV \quad (1.2)$$

In the above expression,  $\alpha$  stands for the property of the fluid dependent on time,  $\mathbf{v}$  is the velocity vector,  $\nabla \cdot$  denotes the divergence operator, and  $dV$  is the volume element over which the integrals are taken.

### 1.3 Mass Conservation

Consider a part of a single-phase fluid with mass 'm' and arbitrary volume 'V'. If the fluid region flows in time, considering a reference frame attached to it, then its dimensions and shape can vary, but its mass remains unchanged. According to the Reynolds transport theorem, by setting the local density as  $\rho(t) = \alpha(t)$ , it's possible to observe the following in the LaGrange reference frame:

$$\frac{\partial \rho}{\partial t} + \nabla \cdot (\rho \mathbf{v}) = 0 \quad (1.3)$$

Where  $\rho$  is the fluid density, and  $\mathbf{V}$  is the velocity vector in the three components  $x, y$  e  $z$ . The operator  $\nabla \cdot$  denotes the divergence operator.

### 1.4 Momentum Conservation

The conservation principle of momentum is derived using Newton's second law. It involves considering a fluid element and a reference frame attached to it (LaGrange coordinates). The temporal variation of momentum is equivalent to the net force acting on the mass element. External forces can be divided into volume forces (e.g., gravitational force and electromagnetic force) and surface forces (such as pressure

forces and viscous forces). If ' $\mathbf{f}$ ' is the resultant force per unit mass, then the net external force ' $\mathbf{F}$ ' acting on a volume of mass ' $\mathbf{V}$ ' is:

$$F = \int_V \rho \mathbf{f} dV \quad (1.4)$$

In general, the surface force is not necessarily perpendicular to the surface on which it acts. For this reason, the surface forces acting on a fluid element must be represented by a second-order tensor  $\sigma$ , known as the stress tensor. The nine components of the tensor are divided as follows: for each coordinate plane, one part is normal to it, and the other two are shear components. The elements of the matrix being the stress tensor are denoted as  $\sigma_{ij}$ , where  $i$  and  $j$  show that the stress acts on the plane  $x_i = \text{constant}$  in the  $x_j$  direction.

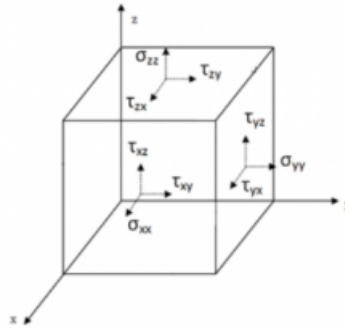


**Figure 1.3:** Tangential stress

Since each part of the surface force acts on a plane  $x_i = \text{constant}$  in the  $x_j$  direction, we can relate the component vector  $p_j$  to the stress tensor:

$$p_j = \sigma_{ij} n_i \quad (1.5)$$

In this expression, ' $p_j$ ' represents the  $j$ -th component of the surface force vector, ' $n_i$ ' is the  $i$ -th component of the unit normal vector to the surface, and ' $\sigma_{ij}$ ' denotes the stress tensor components. The summation convention is assumed in this representation, where repeated indices ( $i$  in this case) imply summation over the range of the coordinate system.

Considering the divergent theorem and assuming the volume is 0, the equation became:

$$\frac{\partial(\rho \mathbf{V})}{\partial t} + \nabla \cdot (\rho \mathbf{V} \otimes \mathbf{V}) = \rho \mathbf{f} \quad (1.6)$$

In this equation,  $\rho$  is the density of the fluid,  $\mathbf{V}$  is the velocity vector,  $\otimes$  denotes the outer product,  $\nabla \cdot$  is the divergence operator, and  $\mathbf{f}$  represents the body force per unit volume acting on the fluid.

## 1.5 Energy Conservation

The principle of energy conservation can be derived using the first law of thermodynamics. Considering the fluid element in motion, its instantaneous energy is the sum of the internal energy per unit mass 'e' and the kinetic energy per unit mass  $1/2 \mathbf{v} \cdot \mathbf{v}$ , where 'v' is the velocity vector.

$$E = \int_V (\rho e + \frac{1}{2} \rho \mathbf{v} \cdot \mathbf{v}) dV \quad (1.7)$$

The temporal variation of total energy, therefore, is given by the variation of work done by external forces and the heat due to conduction. In LaGrange approach and with different assumption the following equation we obtain:

$$\rho \frac{\partial e}{\partial t} + \rho \mathbf{v} \cdot \nabla e = \sigma \cdot \nabla \mathbf{v} - \nabla \mathbf{q} \quad (1.8)$$

## 1.6 Navier Stokes Equations

By introducing the stress tensor with viscous contributions into the equation of conservation of momentum, for a viscoelastic fluid, is possible to derive the Navier-Stokes equation:

$$\rho \left( \frac{\partial \mathbf{V}}{\partial t} + \mathbf{V} \cdot \nabla \mathbf{V} \right) = -\nabla P + \nabla \cdot \sigma \quad (1.9)$$

In this equation,  $\rho$  stands for the density of the fluid,  $\mathbf{V}$  is the velocity vector,  $t$  is time,  $P$  denotes the pressure,  $\nabla$  is the gradient operator, and  $\sigma$  is the stress tensor, which includes both the viscous and elastic contributions. The Navier-Stokes equation describes the motion of a viscous fluid and is fundamental in fluid dynamics, representing the conservation of momentum in the presence of both external and internal forces.

## 1.7 Reynolds Number

The ratio  $\nu = \frac{\eta}{\rho}$  is called the kinematic viscosity and shows the fluid material's tendency tendency to keep non-conservativeness. Additionally, it is interesting to analyze the ratio between inertia forces and viscous forces from the Navier-Stokes equation. This ratio is dimensionless and is shown by the Reynolds number,  $Re$ :

$$Re = \frac{\rho(\mathbf{v} \cdot \nabla)\mathbf{v}}{\eta\nabla\mathbf{v}} = \frac{\rho L\mathbf{v}}{\eta} = \frac{Lv}{\nu} \quad (1.10)$$

Notice the inverse proportionality between the Reynolds number ( $Re$ ) and the kinematic viscosity  $\nu$ . This implies that highly viscous fluids have a low Reynolds number (frictional forces dominate over inertia forces), while non-viscous fluids have a high Reynolds number (inertia forces dominate over frictional forces). The motion of viscous fluids is laminar, and the fluid stratification is caused by viscous forces. On the other hand, the turbulent motion of non-viscous fluids is due to the chaotic motion of fluid particles and is, therefore, generated by inertia forces.

## Chapter 2

# Vehicle Aerodynamics

Vehicle aerodynamics refers to the study and manipulation of the way air flows around a vehicle, such as a car, truck, or any other mode of transportation. It involves understanding how the vehicle's shape, design, and various components interact with the surrounding air. The goal of vehicle aerodynamics is to perfect the movement of air around the vehicle to achieve desired outcomes, such as improved performance, fuel efficiency, stability, reduced noise, and minimized emissions.

Aerodynamic forces, namely drag (resistance to send motion) and lift (upward force), play a crucial role in deciding a vehicle's behavior on the road. Engineers and designers work to shape vehicles in a manner that reduces drag and minimizes lift to enhance fuel economy, increase top speed, and improve overall handling and stability. In the engineering application a nondimensional number, called the drag coefficient ( $C_d$ ), is used;

$$C_d = \frac{F_d}{0.5\rho U^2 A_f} \quad (2.1)$$

Similarly, to what was done for drag coefficient, the lift coefficient can be derived from the nondimensionalization of the force acting perpendicularly at drag:

$$C_l = \frac{F_l}{0.5\rho U^2 A_f} \quad (2.2)$$

At any rate, all aerodynamic effects increase sharply with speed, usually with the square of the speed, and are almost negligible in slow vehicles. Moreover, they are irrelevant in city driving. Aerodynamic effects, on the contrary, become important at speeds higher than 60-70 km/h and dominate the scene above 120-140 km/h. Actually, these figures must be considered only as indications, since the relative importance of aerodynamic effects and those linked with the mass of the vehicle depend on the ratio between the cross-section area and the mass of the vehicle.

At about 90-100 km/h, for instance, the aerodynamic forces acting on a large industrial vehicle are negligible when it travels at full load, while they become important if it is empty.

Vehicle aerodynamics also have a significant impact on various aspects beyond just speed and efficiency. Cooling systems, thermal management of components, passenger comfort (ventilation and noise reduction), and even safety (vehicle stability in crosswinds) is influenced by how air flows around the vehicle. In this chapter, the principal aspects of the interaction of the flow with the car are outlined together with how the flow influence the external aerodynamic of the vehicle.

## 2.1 Streamlines

In aerodynamics, streamlines are imaginary lines that are the continuous path followed by fluid particles (such as air) as they flow around an object or within a fluid flow field. They supply a visual representation of the fluid's motion and direction at any given point. The figure shows the shapes of such streamlines as formed near an airfoil. The visualization of the streamlines can be obtained in the wind tunnel by injecting smoke, pay attention to the density of the color which has to be equal to the one of the air, otherwise it may not follow the streamlines exactly.

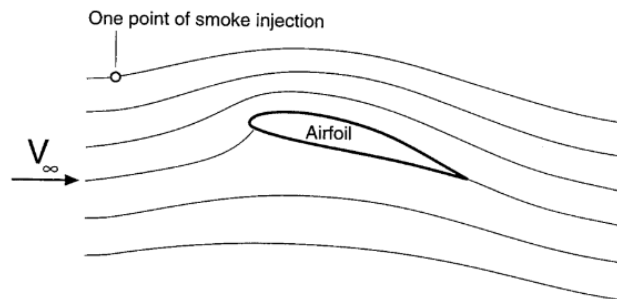


**Figure 2.1:** Streamlines in a steady-state flow

By seeing several streamlines, it is possible to see if the flow follows the vehicle's body shape close to its surface. When the streamlines are close to the solid surface the flow is considered **laminar**, on the contrary if it is not close to the body the flow is considered **separated**.

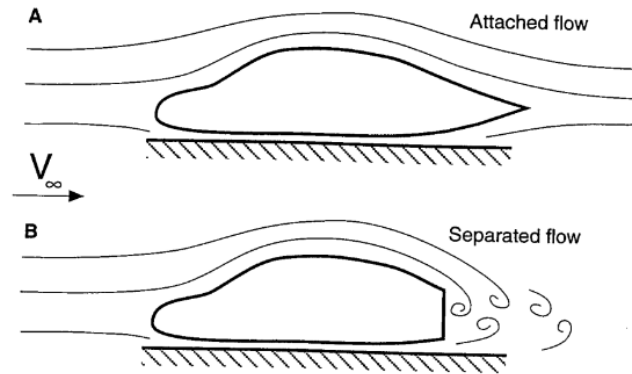


Figure 2.2: Attached and Separated flow

## 2.2 Velocity Distribution

When a vehicle moves through the air, the shape disturbs the air, so the velocity of the flow is not equal at each point. To describe the velocity magnitude, it is possible to use a velocity-distribution diagram like the one below:

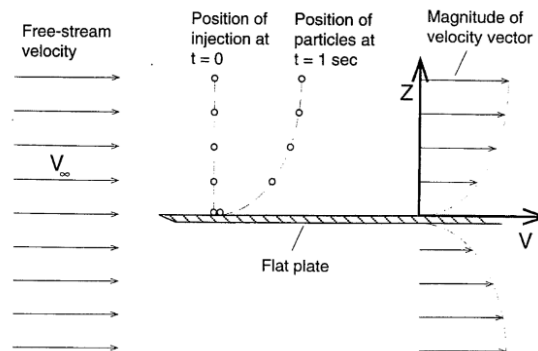
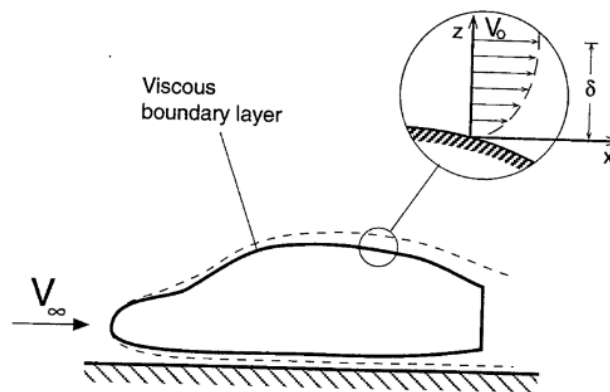


Figure 2.3: Velocity Distribution

Even if the flat surface is parallel to the direction of the flow, it creates a disturbance, leading to have not a uniform distribution along the surface in vertical direction. It's important to notice how the velocity near the shape is zero without any relative velocity, which are important to understand the pressure distribution (**Stagnation point**). Farther away from the shape the velocity increase, up to the local free-stream value. This thin boundary is called **boundary layer**.

## 2.3 Boundary Layer

The boundary layer is a phenomenon in fluid dynamics that comes into play when a fluid flows over a solid surface. Picture of a thin layer of a fluid that sticks to the surface, gradually shifting from the stationary surface to the free stream flow of the fluid farther away. In this process, the initially stationary fluid particles at the surface create what's known as the laminar sublayer. As moving away from the surface, it meets the boundary layer, where the fluid's velocity starts to change. This layer can show two distinct behaviors: a smooth and orderly laminar flow or a turbulent state marked by unpredictable whirls and mixing. The boundary layer's implications are substantial in the realm of aerodynamics, influencing aspects such as drag, lift, and heat transfer. The way it transitions and potentially separates from the surface holds sway over overall system performance.



**Figure 2.4:** Boundary layer

The **transition** point at which the boundary layer transitions from laminar to turbulent flow depends on factors like Reynolds number (a dimensionless parameter related to flow conditions and object size). Turbulent flow is generally more resistant to separation and can better handle adverse pressure gradients. Flow **separation** occurs when the boundary layer loses its attachment to the surface, leading to recirculation zones and increased pressure drag.

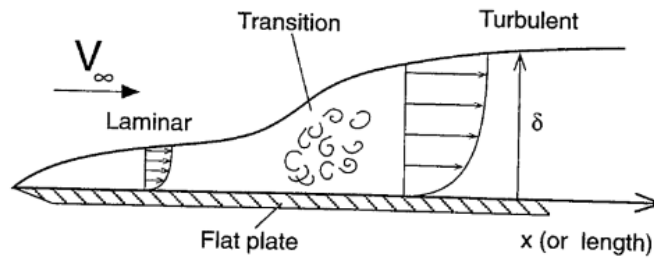


**Figure 2.5:** Variation of boundary layer thickness

Due to the fluctuating turbulent velocity components, the turbulent boundary layer is thicker, therefore, the moment loss in this boundary layer is larger and the turbulent friction is expected to be larger.

## 2.4 Flow: Laminar and Turbulent

Laminar flow is smooth, with layers of fluid moving in parallel. It's orderly and predictable, seen at low speeds or high viscosity. Turbulent flow is chaotic, with irregular movement and mixing. It's common at high speeds or low viscosity. Laminar flow has streamlined paths, low mixing, and low pressure drop. Turbulent flow is chaotic, with high mixing and higher pressure drop.

The change from laminar to turbulent depends on speed, viscosity, and conduit shape. Reynolds number helps predict this transition. Low Reynolds numbers favor laminar flow, high numbers favor turbulent. In engineering, flow type matters for system design and efficiency.

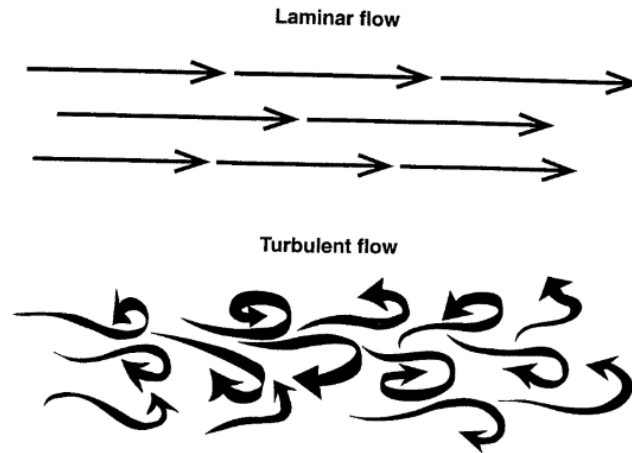


Figure 2.6: Fluid particles in laminar and turbulent flow

## 2.5 Pressure coefficient

After understanding the concept of the velocity distribution, another important parameter in order to evaluate the aerodynamic loads is the pressure coefficient  $C_p$ :

$$C_P = \frac{p - p_\infty}{0.5\rho U_\infty^2} \quad (2.3)$$

Note that the pressure coefficient is a measure of the local pressure  $p$  which is independent of the vehicle speed. Looking in how body shapes affect pressure distribution the following image is used as an example:

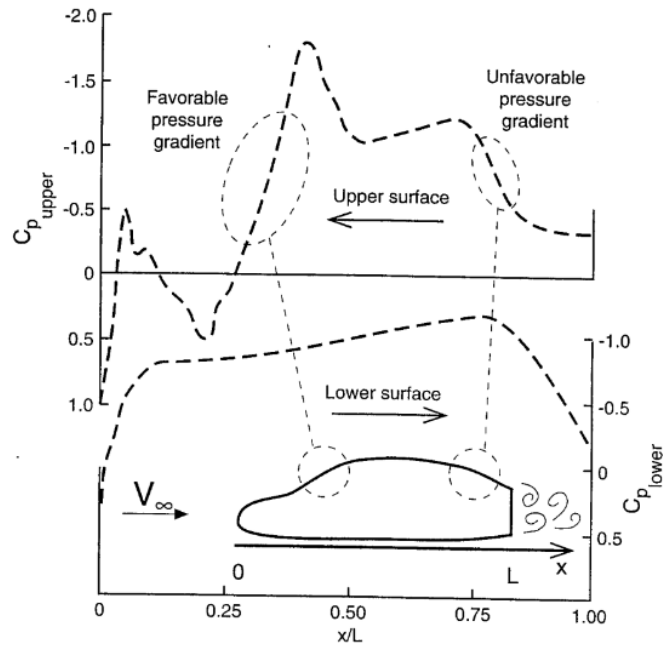


**Figure 2.7:** pressure distribution along the car

Considering a cross-sectional slice through a typical passenger car, you can see the distribution of air pressure around it, as shown in figure. Notably, there's a peak in pressure at the front of the car, which contributes significantly to the drag force. Moving from this point, where there's high pressure and low velocity, the airflow accelerates quickly. However, it soon decelerates just as rapidly when it reaches the windshield.

When the air meets the windshield area, its slowing momentum might not be enough to counteract the resistance posed by a combination of pressure differences and friction with the car's surface. This can lead to the air separating from the car's surface, forming an area where the air circulates back, which in itself contributes to energy loss and consequently, drag.

Moving towards the rear of the car, it can notice an unfavorable pressure gradient. This suggests that the airflow might detach from the car's surface. This separation results in a type of drag known as pressure drag, which adds to the overall resistance experienced by the car as it moves through the air.

## 2.6 Vortex flow

A moving car's aerodynamics can give rise to vortices due to variations in local shear, pressure, or velocity within the flow. These phenomena lead to distinct flow patterns around different car shapes.

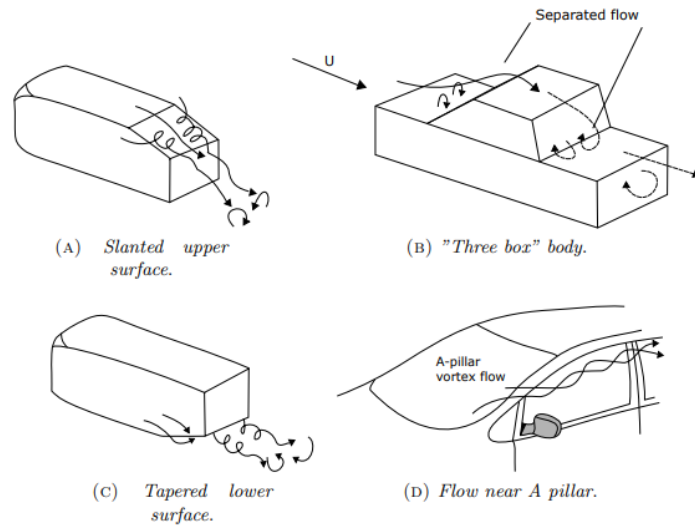


**Figure 2.8:** Vortex flow on generic car shape

The crucial factor in vortex formation involves the emergence of two concentrated vortices along the car's edges. These vortices significantly influence the nearby airflow, resulting in elevated speeds across the surface and generating potent suction forces. This suction effect prompts an increase in lift on the surface, affecting the car's overall aerodynamics.

For instance, when the rear surface of a car slants at an angle between  $10^\circ$  and  $30^\circ$ , two distinct vortices appear. These vortices create heightened velocity along the surface, causing substantial suction forces that amplify lift. In the case of a three-box car body, like a sedan, airflow separation occurs at the joints between the hood and windshield, and at the rear windshield and trunk area. This leads to the formation of a separated pocket of recirculating airflow. This phenomenon influences the vehicle's drag and stability.

Race car designs often incorporate a configuration with a slanted lower rear section. This setup produces two vortices that enhance downforce. This downforce enhances the car's grip and stability at high speeds and while maneuvering corners. The area around the A-pillar generates a vortex that contributes to water accumulation

during motion. Furthermore, the oscillating wake generated by the rear-view mirror can lead to noise issues at high speeds. These vortices result from the separation of airflow, contributing to the formation of the wake behind the car.

The wake area behind a moving car exhibits lower pressure than the surrounding external pressure. This discrepancy, when combined with the higher pressure at the front of the car, contributes to heightened drag resistance. This increased drag resistance negatively affects the vehicle's overall efficiency and fuel consumption.

In summary, grasping the intricate aerodynamic interactions around diverse car configurations is pivotal. These dynamics inform the design process, affecting performance, stability, and efficiency considerations. This knowledge aids in crafting vehicles that align with performance goals and user expectations.

## 2.7 Wheel Aerodynamics

The wheels are one of the most influential components affecting vehicle aerodynamics, responsible at about 25 % of the total drag produced. When examining the airflow around a rotating wheel in the presence of the ground, a distinct pattern of vortices appears, which is illustrated in Figure below:

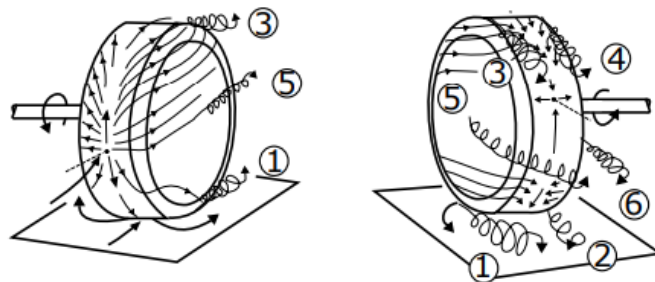


**Figure 2.9:** Vortices around rotating wheel

This pattern consists of three pairs of vortices. The first pair originates from the upper part of the wheel (labeled as 3 and 4), the second pair emanates from the wheel's axis (labeled as 5 and 6), and the third pair forms from the lower region (labeled as 1 and 2). The final pair of vortices, which remain attached to the ground, is referred to as "jetting vortices". In the traditional design of a passenger car, the presence of the wheel arc near the wheel causes three out of these six vortices to dissipate. As a result, only the jetting vortices and the external vortex shedding originating from the wheel's axis persist.

In a study conducted by researchers, it was seen that in the case of a grooved tire, the Venturi effect leads to a sudden drop in pressure at the point where the wheel contacts the ground. On the other hand, with slick tires, the pressure at the same contact point reaches its maximum value. This phenomenon was explained by suggesting that the sudden pressure drop within the tire's grooves encourages air to flow through the tread, resulting in a reduction in the size of the trailing vortices. This shows that different tire designs and configurations can significantly influence the aerodynamic characteristics of the rotating wheel and its interaction with the ground.

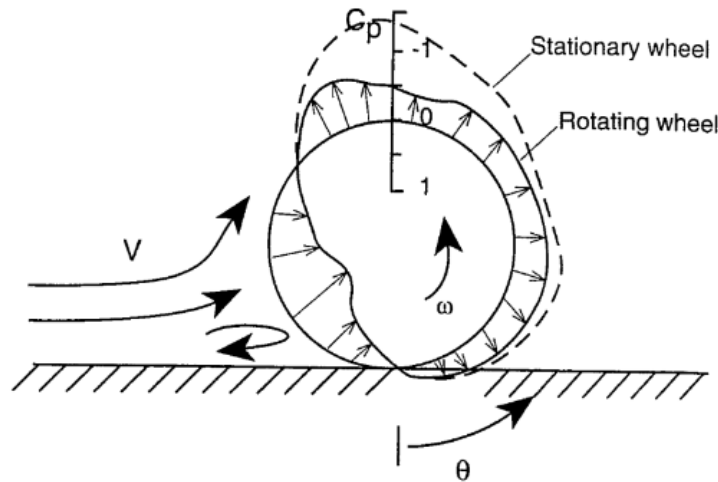


**Figure 2.10:** Pressure distribution on a stationary and rotating wheel

Initial studies delved into the wake created by wheels and the impact of rotation on drag and lift coefficients. These investigations were pivotal in comprehending wheel airflow dynamics. Yet, applying these findings to real-world scenarios proved challenging, as the studies centered on isolated wheels and employed scaled-down models. The evolution of wind-tunnel technology paved the way for more comprehensive examinations.

Recognizing the importance of replicating authentic road conditions and wheel rotation prompted overall enhancements in automotive wind tunnels. Nowadays, a growing number of wind tunnels incorporate various moving-ground systems coupled with proper boundary-layer treatment. This adaptation has brought forth a more intricate airflow environment, particularly within the wheel arches, resulting in reduced overall drag force compared to stationary scenarios. However, this complexity has also introduced challenges in measurement procedures, as forces generated between the tire and moving belt need to be isolated to obtain accurate drag and lift force values.

Furthermore, the heightened complexity of equipment and an improved understanding of wheel flow dynamics have propelled a shift towards more sophisticated models for evaluating vehicle aerodynamic performance. One such method involves accounting for the aerodynamic resistance moment, also known as pumping losses, aerodynamic resistance torque, or ventilation resistance in the literature [6], [18], [19]. This concept acknowledges added forces arising from airflow interaction that can affect a vehicle’s overall efficiency. In essence, the understated role of wheels in vehicle aerodynamics has seen a transformation.

In essence, the understated role of wheels in vehicle aerodynamics has witnessed a transformation. Enhanced simulation techniques and a deeper comprehension of wheel airflow have contributed to refining wind-tunnel practices. The integration of moving-ground systems has led to more accurate assessments of drag and lift forces, albeit with added measurement complexities. Moreover, the move towards intricate models, including consideration of resistance moments, signifies a progressive shift in evaluating vehicle aerodynamic performance.

## 2.8 Forces classification

In dynamic scenarios involving wheel rotation, the forces at play can be categorized into two distinct components: external forces and inertial forces, as depicted in the provided figure.

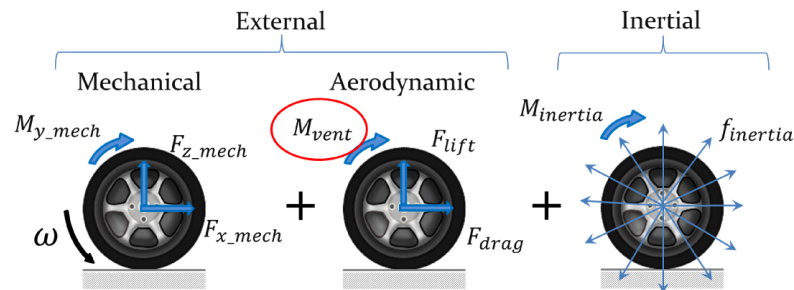
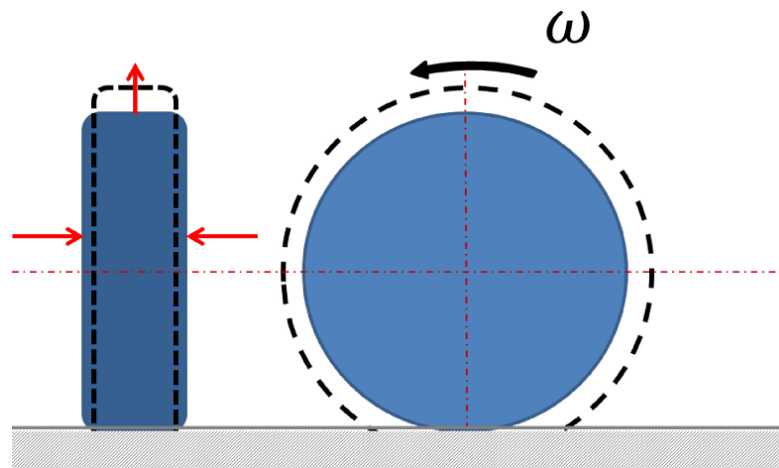


Figure 7 Forces acting on a rotating wheel

**Figure 2.11:** Forces acting on a rotating wheel

The forces at play in the interaction of a rotating wheel with its environment encompass a series of significant aspects. Primarily, it’s essential to consider the concept of inertial forces, which includes the moment of inertia. This latter aspect is an object’s resistance to changes in its rotational speed. These changes, in turn, give rise to forces that counteract this variation, constituting a pivotal element in the wheel’s dynamics.



**Figure 2.12:** Deformations due to inertial forces

Simultaneously, it's important to account for centrifugal forces or distributed inertial forces. These appear from the rotation of the wheel and drive the movement of objects within it outward, reflecting the inertia of these objects. An intriguing side pertains to the alterations that can occur in the geometry of the wheel's tire. These changes arise due to phenomena such as axial compression and radial expansion. Axial compression involves a sort of "flattening" of the tire along its axis of rotation, from both sides. This can lead to substantial shifts in the tire's structure. On the other hand, radial expansion entails an increase in the radial dimension of the tire from its inner to outer regions, a direct consequence of the rotational motion. This form of expansion can significantly affect the overall geometry of the tire, along with inducing a variation in the axis of rotation within the wheel well.

External forces, on the other hand, can be divided into mechanical and aerodynamic components. The aerodynamic components encompass lift, drag, and aerodynamic resistance moments. The latter arise since the wheel is rotating within moving air, generating intricate interactions that influence the system's behavior. The mechanical part, in contrast, encompasses all other elements. Of particular significance is the rolling resistance moment. This moment arises from the non-uniform distribution of pressure in the contact patch between the wheel and the ground while the wheel is in motion. This results in a slight forward shift of the equivalent normal force compared to the wheel's center. This shift gives rise to the so-called rolling resistance moment, which is a fundamental aspect to consider in the analysis of the forces involved in the system.

Ventilation resistance  $M_{vent}$  is sometimes referred to as pumping losses, ventilation torque, or ventilation resistance, similar to aerodynamic drag force. This resistance is governed by the pressure part, which arises due to the non-uniform distribution of normal pressure around the wheel and the viscous part, originating from the surface friction acting on different rotating parts. In the context of the wheel, the rotating parts include the tire, the rim, and the brake disc. Consequently, the ventilation moment acting on the wheel is closely tied to the geometric configuration and dimensions of these components. The comprehension of this phenomenon needs a meticulous analysis of the morphological and kinematic characteristics of the moving parts, as they exert a considerable influence on the manifestation and magnitude of ventilation resistance.

## Chapter 3

# Computational fluid dynamics

This chapter presents the primary mathematical frameworks employed within commercial Computational Fluid Dynamics (CFD) software for analyzing the movement of fluid around an object. The behavior of the fluid is characterized by partial differential equations, specifically the Navier-Stokes equations. However, solving these equations analytically is only possible under simple circumstances. Computational Fluid Dynamics offers an avenue to derive an approximate numerical solution through discretization techniques, wherein the intricate differential equations are approximated through a set of algebraic equations. Each cell will be evaluated for its flow field, and boundary conditions will be imposed.

This division process is referred to as discretization using the finite volume method. When the Navier-Stokes equations are solved directly for each individual volume, it is termed Direct Numerical Simulation (DNS), which is highly faithful to reality but demands immense computational power, often referred to as a "killer application." An alternative to DNS, though less correct, faster, and more cost-effective, is the use of Reynolds Averaged Navier-Stokes equations (RANS).

### 3.1 Reynolds Averaged Navier-Stokes Equation

To statistically represent a fluid flow by solving the governing equations, the traditional approach in Computational Fluid Dynamics (CFD) is to resort to the simplified Reynolds-Averaged Navier-Stokes (RANS) equations. The RANS equations are the time-averaged form of the standard Navier-Stokes equations, where quantities are no longer instantaneous but are averaged over a certain period, sufficiently minor compared to the phenomena being studied and sufficiently

large compared to turbulence disturbances. Turbulent motion can be seen as a combination of mean motion and time-varying fluctuation:

$$u_i(t) = U_i + u'_i(t) \quad (3.1)$$

where the second term is the fluctuating one, typically orders of magnitude smaller than the mean term, that's the time average of velocity instantaneous values. The Reynolds-Averaged Navier-Stokes equations are derived by applying Reynolds decomposition, which involves breaking down quantities dependent on time into averaged terms and fluctuating terms:

$$U_i = \langle u_i(t) \rangle = \lim_{T \rightarrow \infty} \frac{1}{T} \int_0^T u_i(t) dt \quad (3.2)$$

By reformulating the Navier-Stokes equations for a compressible flow and by averaging each equation over time, we acquire:

$$\frac{\partial U_i}{\partial x_i} = 0 \quad (3.3)$$

$$\frac{\partial u'_i}{\partial x_i} = 0 \quad (3.4)$$

$$\frac{\partial u_i}{\partial t} + U_j \frac{\partial u_i}{\partial x_j} = -\frac{1}{\rho} \frac{\partial P}{\partial x_i} + \mu \frac{\partial^2 u_i}{\partial x_j \partial x_j} - \frac{\partial \langle u'_i u'_j \rangle}{\partial x_j} \quad (3.5)$$

where the last component represents represent the Reynolds stresses. Appearing from the intricate dance of momentum within fluctuating velocity fields, Reynolds stresses take on the form of a second-order tensor.

The diagonal elements  $\langle u'_i u_j \rangle$  give birth to normal stresses, while the off-diagonal elements embody shear stresses. The Reynolds stress tensor preserves symmetry,  $\langle u'_i u'_j \rangle = \langle u'_j u'_i \rangle$ . The new configuration unfurls with four equations wrestling against the enigma of thirteen unknowns. This captures the heart of the closure problem, a puzzle demanding resolution.

Hence, addressing this conundrum beckons for more than mere equations; it beckons for insights. This underscores the pivotal significance of deciphering the Reynolds stresses through thoughtfully tailored methodologies.

## 3.2 Modelling Turbulence

Modeling turbulence is a crucial process to accurately describe and simulate the real behavior of a fluid. To be able to compute turbulent flows using Reynolds-Averaged Navier-Stokes (RANS) equations, it becomes essential to develop turbulence models capable of predicting Reynolds stresses and scalar transport terms. This modeling can take various forms, and the accuracy of the representation is directly related to the amount of computational resources required. The most common RANS turbulence models are typically classified based on the number of additional transport equations introduced:

- Equation model: **Mixing Length model**;
- One-equation model: **Spalart-Allmaras**;
- Two-equation models: **k-epsilon**("standard"), **k-omega**("Wilcox"), **SST**(Menter);
- Seven-equation model: **Reynolds Stress model**.

All models, except for the Reynolds stress model, rely on the Boussinesq approximation. Joseph Boussinesq, in fact, experimentally deduced that turbulence decreases when there's shear stress present in incompressible isotropic flows. Moreover, what I find intriguing is how turbulence increases as the average rate of deformation rises. To make the equation system comprehensive, it's essential to establish a connection between Reynolds stress and the average rate of deformation. This relationship is expressed in the following form:

$$\tau_{ij} = \mu_t \left( 2S_{ij} - \frac{2}{3} \frac{\delta u_k}{\delta x_k} \delta_{ij} \right) - \frac{2}{3} \rho k \delta_{ij} \quad (3.6)$$

where  $S_{ij} = \frac{1}{2} \left( \frac{\partial u_i}{\partial x_j} + \frac{\partial u_j}{\partial x_i} \right)$  is the mean rate of strain tensor, while the second term  $k = \frac{1}{2} u'_i u'_i$  represents the turbulent kinetic energy. What characterizes this as an approximation is the assumption of the turbulent kinematic viscosity as an isotropic scalar quantity. Various models are then designed to estimate this turbulent viscosity.

### 3.3 K- $\varepsilon$ standard method

The  $k - \varepsilon$  turbulence model appears as the most extensively employed mathematical framework within the domain of computational fluid dynamics, specifically designed for the simulation of averaged behaviors showed by turbulent flows. Classified as a representative of two-equation models, it supplies a comprehensive portrayal of turbulence by a pair of coupled partial differential equations that govern the transport of turbulent kinetic energy( $k$ ) and turbulent dissipation rate( $\varepsilon$ ).

Diverging from its predecessors, the  $k - \varepsilon$  directs its attention towards the intricate mechanisms that significantly influence the behavior of turbulent kinetic energy. This inherent emphasis on the turbulent kinetic energy imparts a heightened level of generality when compared to models grounded in the concept of mixing length. At its fundamental premise lies the assumption that turbulent kinetic energy possesses isotropic characteristics, indicating that the relationship between the Reynolds stress tensor and the mean strain tensor remains consistent across all spatial directions.

$$\frac{\partial \rho k}{\partial t} + \frac{\partial(\rho k u_i)}{\partial x_i} = \frac{\partial}{\partial x_j} \left[ \frac{\mu_t}{\sigma_k} \frac{\partial k}{\partial x_j} \right] + 2\mu - t E_{ij} E_{ij} - \rho \varepsilon \quad (3.7)$$

$$\frac{\partial \rho \varepsilon}{\partial t} + \frac{\partial(\rho \varepsilon u_i)}{\partial x_i} = \frac{\partial}{\partial x_j} \left[ \frac{\mu_t}{\sigma_\varepsilon} \frac{\partial \varepsilon}{\partial x_j} \right] + C_{\varepsilon 1} \frac{\varepsilon}{k} 2\mu_t E_{ij} E_{ij} - C_{\varepsilon 2} \rho \frac{\varepsilon^2}{k} \quad (3.8)$$

where  $u_i$  signifies the velocity component in the respective direction,  $E_{ij}$  embodies the strain rate tensor component, and  $\mu_t$  represents turbulent viscosity defined as:

$$\mu_t = \rho C_\mu \frac{k^2}{\varepsilon} \quad (3.9)$$

these equations encompass certain constants, referred to as calibration constants, derived from experimental findings. Standard values often employed are:

$$C_{\varepsilon 1} = 1.44, \quad C_{\varepsilon 2} = 1.92, \quad C_\mu = 0.09, \quad \sigma_k = 1.0, \quad \sigma_\varepsilon = 1.3 \quad (3.10)$$

The  $k - \varepsilon$  turbulence model offers numerous advantages in terms of its implementation: it is relatively easy to apply and demonstrates convergent calculations with notable stability. This model can supply reasonably correct predictions for a wide range of flows, covering multiple situations and scenarios within computational fluid dynamics.

However, it is important to highlight some limitations of the model. Unlike simpler models based on mixing length, the  $k - \varepsilon$  model requires a higher amount

of memory due to the need to solve two additional equations. This can result in increased computational demand and limit its applicability in resource-constrained contexts.

Furthermore, the model is less accurate in situations involving significant adverse pressure gradients, such as in compressors, where prediction issues can arise. Additionally, the model does not fare well in flows with pronounced separations or asymmetric jets, where its approximation might be less effective. Further limitations arise in more complex situations, such as flows with curved boundary layers or rotational flows. In these circumstances, the discrepancy between the model and reality can increase, reducing its capability for accurate prediction.

### 3.4 Large Eddy Simulation

Another distinct approach in simulating turbulent flows is known as Large Eddy Simulation (LES). In this framework, the focus is directed towards the emulation of exclusively the dominant large-scale motions present in the inertial range, as they show significantly higher energy levels compared to their smaller-scale counterparts. Moreover, these large-scale motions play a pivotal role in the transport of conserved properties. It is worth noting that LES is particularly suited for scenarios characterized by high Reynolds numbers or intricate geometric configurations. Delving into the theoretical foundations of Large Eddy Simulation (LES), it can delineate four distinct conceptual phases that underlie this approach.

First and foremost, the velocity field  $U(x, t)$  is partitioned into two distinct components: the filtered component  $U(x, t)$ , which encapsulates the behavior of large-scale turbulent structures, and the sub-grid scale residual component  $u_0(x, t)$ . The filtered component  $U(x, t)$  manifests as a three-dimensional and dynamically varying representation of the motion of significant large-scale turbulent structures.

The evolution equations governing the behavior of the filtered velocity field are rigorously established. These equations are derived directly from the fundamental Navier-Stokes equations. Particular attention is directed towards the momentum equation, which incorporates the residual stress tensor (commonly known as the sub-grid scale stress tensor).

To achieve a comprehensive closure relation, a modeling procedure is required for the sub-grid scale stress tensor. Often, this is realized through the adoption of a turbulent viscosity model, which characterizes the interaction between turbulent motions at the large and small scales.

The filtered equations, solvable numerically, are subsequently addressed to determine the profile of  $U(x, t)$ . This process ultimately yields an accurate approximation of large-scale turbulent motions, underscoring the efficacy of the method in comprehending and simulating complex and variable flows.

It is pertinent to highlight that analogous procedures can be extended to encompass the pressure field, contributing to a comprehensive LES framework.

### 3.5 Detached Eddy Simulation

The Detached Eddy Simulation (DES) approach serves as an intriguing amalgamation of two pivotal techniques in computational fluid dynamics: Reynolds-Averaged Navier-Stokes (RANS) and Large Eddy Simulation (LES). The foundation of DES lies in the Spalart-Allmaras one-equation turbulence model, a prominent choice in modeling turbulent flows.

In a broader sense, delving into the specifics of grid-based modeling, it's possible to encounter a pivotal distinction between RANS and DES. In the realm of RANS, the characteristic length scale "d" is typically defined as the distance from the nearest wall. In the context of DES, however, this characteristic length "d" takes on a nuanced meaning. It becomes the minimum between the distance from the wall and a length that is proportionally connected to the local grid spacing. This distinctive approach is mathematically captured through the expression:

$$d_{DES} = \min(d, C_{DES}\delta) \tag{3.11}$$

where  $C_{DES}$  is a model constant and  $\delta$  stands for the local grid spacing. For structured grids, this  $\delta$  translates to the maximum grid spacing across all spatial dimensions. On the other hand, for unstructured grids, it generally corresponds to the maximum edge length linking the centroids of neighboring cells.

One of the fundamental principles underpinning DES revolves around the careful partitioning of the computational domain. Boundary layers and regions characterized by irrotational flows are treated using the well-established RANS closure model. Yet, the intrigue of DES appears from the inherent modification of the turbulence model itself. Under the right conditions—specifically when the grid resolution is fine enough—the turbulence model undergoes a transformation, adopting qualities akin to a basic LES sub grid scale model within detached flow regions. This is where the essence of DES truly shines.

By embracing this approach, the simulation encapsulates the strengths of both RANS and LES methodologies. It captures the intricacies of boundary layer phenomena while simultaneously venturing into the realms of unsteady separated flows, combining the stability of RANS with the resolution power of LES.

### 3.6 Direct Numerical Simulations

Direct Numerical Simulation (DNS) is an advanced modeling approach within the realm of computational fluid dynamics that aims to capture detailed and accurate fluid dynamic phenomena in a given problem. Unlike other simulation methods that rely on approximate models, DNS directly solves the Navier-Stokes equations in all their components and details, without resorting to modeling schemes to be turbulence or other complex physical processes:

$$\frac{\partial u}{\partial t} + (u \cdot \nabla)u = -\frac{1}{\rho}\nabla p + \nu\nabla^2 u \quad (3.12)$$

In DNS, this equation is pivotal as it lies at the core of the simulation process. It encapsulates the dynamics of fluid flow by accounting for the temporal evolution of velocity, the convection of flow properties by the flow itself, the impact of pressure, and the diffusive effects caused by the fluid's viscosity. This equation is central to the simulation's goal of capturing the intricate interactions and behaviors present in turbulent flows. It's worth noting that this equation is discretized and solved numerically over a computational domain in DNS. The equation's terms capture various physical phenomena that contribute to the complex behavior of turbulent flows.

The distinctive aspect of DNS is its ability to consider both macroscopic and microscopic quantities of the flow. This means that vortices of all sizes, ranging from the scales of the largest structures to the exceedingly small scales typical of viscous interactions, are fully captured by the simulation. This makes DNS extremely accurate in cases where a detailed understanding of flow dynamics is required, such as in complex flows, separations, body interactions, and more.

However, there is a notable drawback associated with the use of DNS: it requires significant computational resources. Since DNS resolves all scales of the flow, it needs a fine resolution grid and very small-time steps to accurately be the temporal evolution of the flow. This incurs a high computational cost, which can limit the applicability of DNS to problems of limited size or substantial computational resources. Furthermore, DNS is more suitable for steady flows or flows where temporal fluctuations are negligible. For transient or unsteady flows, the requirement for a very small-time step can become a significant computational challenge.

### 3.7 Methods comparison

In the realm of fluid dynamics simulations, both Large Eddy Simulation (LES) and Direct Numerical Simulation (DNS) stand out for their potential to supply heightened accuracy when compared to models rooted in the Reynolds-Averaged Navier-Stokes (RANS) equations. Particularly, DNS emerges as a meticulously detailed simulation approach within the field of fluid dynamics. It involves solving the Navier-Stokes equations directly, bypassing the need for turbulence models. This method proves adept at capturing vortices across all dimensions.

However, the computational power demanded by DNS is notably substantial, even for relatively straightforward flows. The overall cost, encompassing temporal steps, can be significant, often scaling around  $Re_L^3$ . As such, DNS isn't ideally suited for industrial applications, given the current limitations in available CPU resources, making it predominantly a research tool.

LES method offers a remedy to the limitations of RANS simulations. It proves especially valuable when accuracy is a concern or when simulating unsteady scenarios. It belongs to the realm of Scale Resolving Simulations (SRS), which essentially means that while it resolves large-scale vortices, it models smaller-scale ones. The definition of what constitutes a "large" or "small" vortex hinge on the physical dimensions of the flow geometry and the Reynolds number. The smaller vortices find their explanation through reference to the Kolmogorov scale.

The primary motivation for employing Large Eddy Simulation (LES) models lies in the fact that large-scale vortices handle 90% of mass transport, momentum, and energy transfer, thus directly influencing the average flow behavior. Smaller vortices, on the other hand, primarily contribute to fluctuations dissipation. The main drawback, however, is that LES demands substantial computational power (less than DNS but still considerable) due to the need for a high-resolution grid and very small-time steps for non-stationary simulations. The RANS (Reynolds-Averaged Navier-Stokes) model, on the contrary, is applied to problems requiring a stationary solution. Moreover, with sufficiently refined grids, precision reaches satisfactory levels. Nevertheless, these considerations become less valid in more complex scenarios.

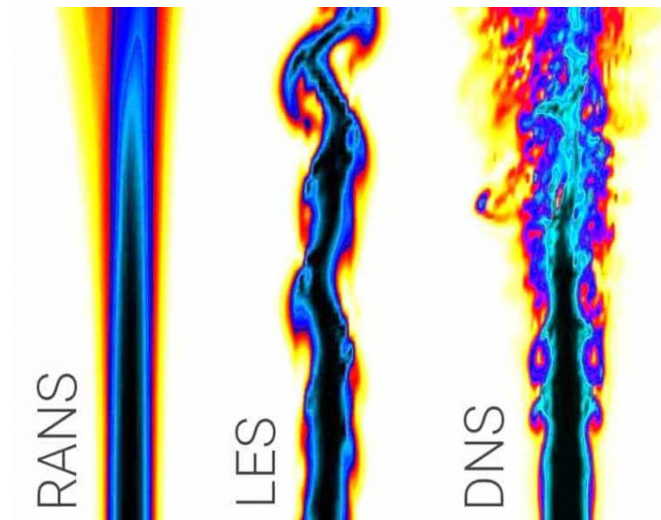


**Figure 3.1:** Comparison of Simulation Methods

The case depicted in the above image is arbitrary, aimed at highlighting the significant precision disparity between LES and RANS. While DNS can capture all the effects of a phenomenon, the LES method focuses on larger-scale vortices and neglects smaller ones. The choice of turbulence model depends on the nature of the phenomenon and simulation requirements.

## Chapter 4

# Wind Tunnel

A wind tunnel is a device used to investigate how a fluid, typically air, behaves around an object. The analysis conducted in an aerodynamic tunnel is facilitated by the principle of reciprocity. This principle states that the aerodynamic forces generated by a body in motion at a velocity  $V$  in still air are equivalent to those generated by a stationary body exposed to a flow with velocity  $V$ . The need to conduct experiments on scaled-down models has given rise to the concept of similarity with real systems, to figure out the responses of the models and the degree of accuracy of their approximations.

The following dimensionless quantities are taken into account:

$$\text{Ma} = \frac{V}{\sqrt{kRT}} \quad (4.1)$$

$$\text{Re} = \frac{\rho V L}{\mu} \quad (4.2)$$

$$\text{Fr} = \frac{V}{\sqrt{gL}} \quad (4.3)$$

The aim of similarity is to set up a correspondence between a scaled model and a real prototype in order to extract relevant information for flow analysis. However, achieving complete similarity, where all dimensionless parameters and geometric characteristics coincide, is often impractical. Therefore, a partial similarity is often chosen, focusing on the aspects relevant to the specific experimental application.

The application of dimensionless numbers, such as the Reynolds number for viscous and incompressible flows in the subsonic regime, the Mach number for transonic, supersonic, and hypersonic flows where compressibility is significant, and the Froude number for gravitational flows, helps set up relationships between the scaled model and the real system.

A preliminary categorization of wind tunnels is based on their ability to manipulate the velocity field:

- Subsonic wind tunnels (Mach number  $Ma < 0.8$ );
- Transonic wind tunnels ( $0.8 < Ma < 1.2$ );
- Supersonic wind tunnels ( $1.2 < Ma < 5$ );
- Hypersonic wind tunnels ( $Ma > 5$ ).

Two main categories of wind tunnels can be distinguished: open circuit and closed circuit. Each consists of a converging section, a nozzle guiding the flow to the test section, and a diverging section. Additionally, fans, grids, and screens are used to homogenize the flow and minimize turbulence.

Open circuit wind tunnels are less intricate but tend to be noisier and less efficient. The fan pulls in ambient air and then expels it through a diverging section. This limits the use of pre-existing moving air. However, they offer cost and maintenance advantages, bypassing the need for elaborate conditioning systems.

Closed circuit wind tunnels, though costlier to prove and keep, ensure superior air quality, reduced acoustic pollution, and lower energy consumption compared to open tunnels with the same test section area. Designing duct curves and managing temperature increases due to air movement and friction are critical. A conditioning system stabilizes temperature, affecting pressure, fluid density, and Reynolds number.

Another classification is based on the test section integration. If the test section aligns with the converging and diverging sections, it's termed "closed." Otherwise, it's labeled "open." Automotive wind tunnels usually adopt open circuits with a longitudinal dimension exceeding the transverse. This minimizes the blocking effect and mitigates pressure gradients along the fluid flow. This adjustment counters the "buoyancy" effect, where the body appears to float within the flow, potentially altering the drag coefficient ( $C_x$ ).

Initially, aeronautical wind tunnels incorporated a ground plane to mimic road conditions. Subsequently, dedicated automotive wind tunnels appeared, featuring a stationary ground. However, research progressed, affirming the essential role of rotating wheels and advanced moving-ground simulation systems for correct on-road emulation. The concept of a moving belt to replicate authentic boundary conditions beneath vehicles isn't novel, but it has undergone substantial evolution. The concept of a moving belt to replicate authentic boundary conditions beneath vehicles isn't

novel, but it has undergone substantial evolution. This section delves into diverse moving-ground systems employed in automotive wind tunnels.

## 4.1 Single belt system

Within the context of automotive aerodynamic experimentation, a distinctive system appears that of the moving belt positioned beneath the vehicle. This system, characterized by a belt of larger dimensions and greater extension than the model under examination, is accompanied by a suction mechanism equipped with openings and distributed suction zones.

The aim is to remove the air confined within the underlying boundary layer before it interacts with the moving belt. This combination of elements generates an almost best flow in the region beneath the vehicle. This configuration finds favor in the realm of racing car development, underscoring its suitability in such a domain.

However, it should be noted that this system presents constraints. In practice, it is necessary to suspend the vehicle using a cable, which can be found either at the top or the rear of the vehicle, with the force balance typically housed within the model. This cable, subjected to the weight of the model, can be of considerable size, triggering interference phenomena that affect force measurements.

Additionally, a challenge arises in distinguishing between wheel rolling resistance and aerodynamic drag. This is because the wheels come into contact with the moving belt. One possible solution involves the adoption of separate arms for each wheel, as depicted in the illustration.



**Figure 4.1:** Single belt moving ground set-up

This approach allows for the complete isolation of the wheels from the model and circumvents issues in measuring aerodynamic forces on the vehicle body. Separate balances can be employed to measure forces acting on the rotating wheels. The interference effect stemming from the wheel arms must also be taken into consideration.

## 4.2 Five-belt system

In this configuration, the vehicular system manifests a distinctive structural arrangement characterized by its reliance upon four strategically positioned struts that supply foundational support beneath its chassis. This innovative design obviates the necessity for a conventional overhead support mechanism.

A salient purpose of this structural setup is to ease the unimpeded rotation of the vehicle's wheels. To this end, these wheels are situated atop diminutive belts or rollers, often referred to in the technical parlance as "Wheel Drive Units" (WDUs), an acronym derived from the English term.



**Figure 4.2:** 5-belt moving ground set-up

It is imperative to underscore the interconnectedness of these WDUs and the vehicle struts with the broader vehicular equilibrium. Notably, this equilibrium part is strategically found within the subterranean expanse of the testing section. This judicious arrangement affords the opportunity for a direct measurement of the aerodynamic drag force without the confounding influence of rolling resistance.

In the pursuit of simulating the complex dynamics of vehicular movement over a

mobile substrate, a large central belt has been incorporated that spans the underbelly of the vehicle. It is, however, essential to delineate the inherent limitations of this design. The disposition of the vehicle struts restricts the width of the central belt, impeding its comprehensive coverage of the entire underbody. Consequently, a localized alteration of the surrounding airflow regime is conceivable. As a countervailing measure, strategies such as tangential insufflation and distributed boundary-layer aspiration have been proposed. Additionally, a judicious measure of caution is warranted, as the very struts that serve as the fulcrum of support can inadvertently introduce subtle interference effects that could impinge upon the precision of force measurements obtained during experimental endeavors.

### 4.3 Aeroacoustics Gallery in Orbassano

The eco-chamber aerodynamics facility at FCA, operational since 1976, is a closed-circuit structure modeled on the Gottingen design, featuring a rectangular layout. The test chamber follows a  $\frac{3}{4}$  open design and is purposefully designed to accommodate life-sized 1:1 scale vehicle. Its functionality aligns with that of a subsonic wind tunnel, capable of reaching speeds that exceed 200 km/h. Initially conceived with a relatively uncomplicated configuration, over the years, it has undergone a series of enhancements encompassing both aerodynamic and acoustic aspects.

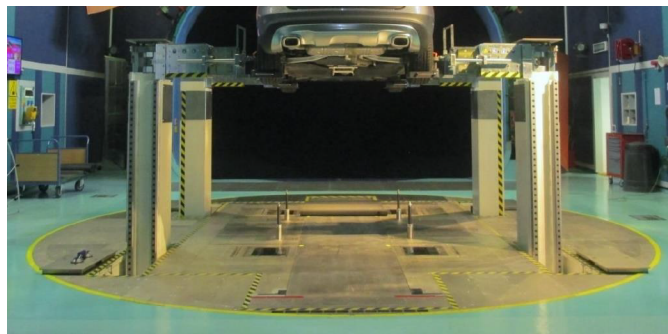


**Figure 4.3:** Rotating Platform

Significant updates have included the integration of a balance system in the 1980s, the abatement of background noise through the incorporation of sound-absorbing panels, and the implementation of a noise evaluation system based on beamforming to refine acoustic testing in the 2000s. Further, in 2014, a momentous transformation ensued, involving the replacement of the entire weighing platform with a novel setup featuring the Rolling Road Simulation System, replete with a comprehensive five-belts installation, all synergized with a modernized balance

system. Within the facility, there is an integrated vehicle lift mechanism designed to ease alterations to the underbody during testing sessions.

## 4.4 Rolling Road Simulation System

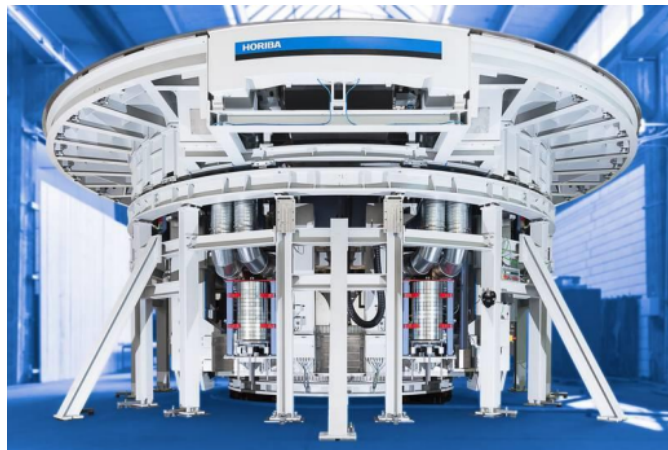


**Figure 4.4:** Platform

The RRS system, acronym for "Rolling Road System," is a fundamental component in vehicle aerodynamic and dynamics testing. In short, its primary purpose is to simulate real driving conditions for a vehicle within a controlled environment inside a test chamber. Below, we will delve into its functions and the reasons for its use in more detail.

### Measuring Aerodynamic Forces and Moments

When a vehicle is in motion, the surrounding air exerts forces and moments on it. These factors influence the vehicle's stability, grip, and overall performance. The RRS system is designed to accurately measure these forces and moments as the air interacts with the vehicle. These measurements are essential for assessing and perfecting the vehicle's aerodynamics, aiding in reducing air resistance and enhancing fuel efficiency.

### Simulating Wheel and Road Movement

The second primary function of the RRS system is to simulate the movement of the vehicle's wheels and the road surface beneath it. When a vehicle travels along a road, its wheels rotate while the road surface moves underneath. This movement

affects rolling resistance and the vehicle's dynamic behavior. The RRS system looks to replicate this condition by simulating the movement of the wheels and the pavement within the test chamber.

### Why Simulate Wheel and Road Movement?

- **Realistic Testing Conditions:** Using the RRS system allows designers and engineers to evaluate a vehicle in conditions that closely resemble real-world driving, as opposed to a stationary vehicle on a fixed platform. This helps in obtaining more correct and representative data regarding the vehicle's performance in actual driving situations.
- **Performance Optimization:** Simulating the movement of wheels and the road surface aids in evaluating the vehicle's behavior in terms of grip, handling, and ride comfort. This enables engineers to perfect aspects such as suspension, tires, and other vehicle components to ensure a safe and comfortable driving experience.
- **Accurate Aerodynamic Testing:** Accurately measuring aerodynamic forces in conditions that include wheel movement is critical for improving the vehicle's aerodynamics, thereby reducing air resistance and enhancing fuel efficiency.

## 4.5 Use of Mini Belts in Wind Tunnel Testing

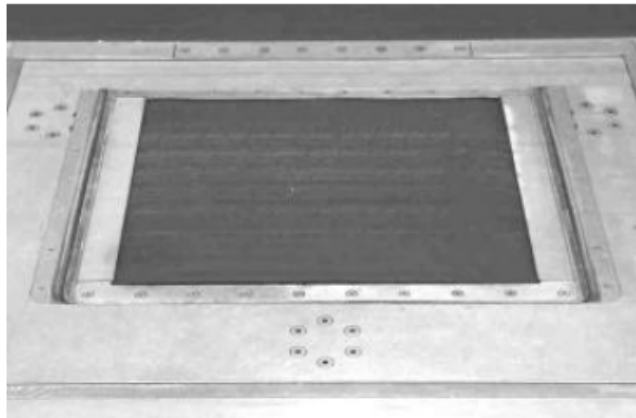


**Figure 4.5:** Mini belt

In wind tunnel testing, mini belts play a significant role in measuring and analyzing the forces acting on a model vehicle. These mini belts, typically part of the model, help transfer the forces experienced by the model to the wind tunnel

balance. Added struts are often used to stabilize the vehicle within the test setup. Both the mini belts and struts are strategically placed on the balance platform, ensuring that all forces and moments affecting the model are effectively channeled to a single sub-frame.

This approach cuts internal forces and facilitates the integration of forces and moments, regardless of the distribution of loads at various contact points. The boundary between the loaded and unloaded areas is defined by the gap between the mini belt and the floor of the test section. Consequently, mini belts replace conventional balance pads in this setup.

However, this method has a drawback. The airflow around the rotating wheels creates an unintended lift force on the mini belts, leading to inaccuracies in the balance measurements. To address this issue when wheels are stationary, one can measure the pressure distribution around the wheels on the pad surfaces and use the average value to calculate the vertical force, which should then be subtracted from the measured lift force.

Another technique for deciding the required pad correction involves using smaller pads that precisely match the tire patch size in the same wind tunnel. Nevertheless, both methods are applicable only when the wheels are stationary. Measuring the static pressure accurately on a moving surface is challenging, and using pads as small as the tire patch is impractical when simulating rotating wheels.

When simulating rotating wheels, it is essential to keep adequate distances between the wheels and the fixed part of the wind tunnel floor to ensure reliable flow simulation. Given these challenges, a computational approach seems to be the most viable way to determine the correction needed for cases involving rotating wheels. The accuracy of this Computational Fluid Dynamics (CFD) approach can be verified by comparing it to measured data obtained with stationary wheels.

An advantage of the new setup, where rotating wheels rest on mini belts, is that the wheels are precisely aligned with the center of the pad surfaces. If the primary influence on the flow characteristics is attributed to the tires themselves rather than the vehicle's shape, the pressure distribution around the tire contact patch tends to be consistent across various vehicles and primarily depends on the tire dimensions. This consistency allows for a tabulated approximate correction for the pads, potentially cutting the need for individual pressure measurements on the pad surfaces.

# Chapter 5

## CFD Analysis

As said in the previous chapters, the purpose of this study is to investigate the aerodynamics drag, adopting different wheels position on the Mini belts. The goal is to find which are the correlations between the numerical tests and the wind tunnel test, in order to obtain the low possible, drag which has a big impact on the CO2 value too. The software we are going to use are ANSA and Star-CCM+. Main setting, such as meshes parameters and boundary conditions, are also reported. The ANSA pre-processor software, from BETA company, was used in the pre-processing analysis for CAD model preparation and surface mesh. STAR-CCM+® software, from SIEMENS company, was used for fluid dynamics simulations.

### 5.1 Mesh Generation

The mesh, in general terms, is a three-dimensional or two-dimensional grid of finite elements that subdivides the domain of a problem into small regions. In ANSA, a widely used pre-processing software in the field of numerical simulation, the creation and management of the mesh are fundamental for preparing a model for numerical simulation, especially for Computational Fluid Dynamics (CFD) and Finite Element Analysis (FEA). In a simulation environment, especially when working with meshing software like ANSA, various issues related to the quality and compliance of the mesh can arise. Below, we will discuss some of the most common problems that may occur during mesh preparation:

- Duplicate Elements: This issue occurs when there are mesh elements that overlap or significantly intersect. Duplicate elements can lead to inaccurate simulation results and must be identified and resolved;
- Penetrations: Penetrations occur when mesh elements pass through surfaces or overlap in a non-physical manner. This can result in serious errors in the simulation

and must be corrected to obtain reliable results;

- **Single or Triple Cons:** These problems relate to connection points in the mesh. "Single Cons" refers to a connection point between three elements, while "Triple Cons" refers to a connection point between a single element and three points. These can cause instability in the mesh and need to be addressed;

- **Non-Manifold Mode:** Non-manifoldness is a condition where a point has more than two adjacent elements. This situation can lead to errors in the simulation and must be tackled to ensure a valid mesh;

- **Collapse Points:** Collapse points occur when multiple mesh points overlap at the same location in three-dimensional space. This can compromise the quality of the mesh and should be avoided or resolved.

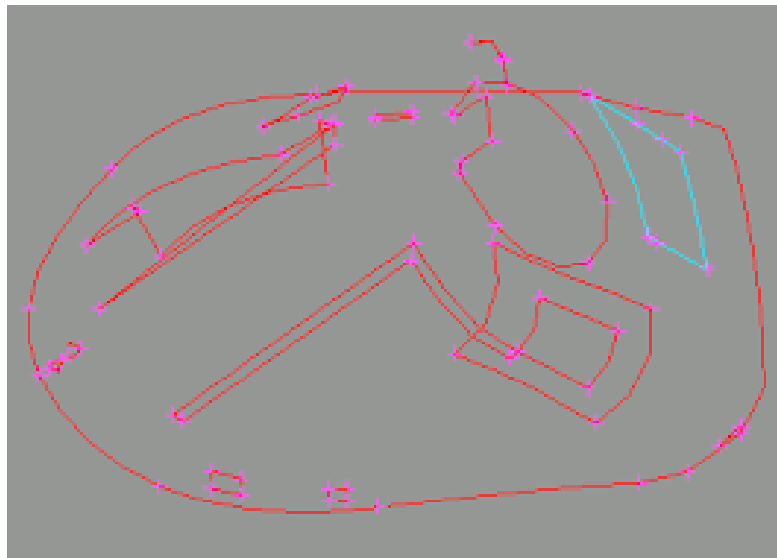


**Figure 5.1:** Example of Mesh error: Single and Triple Cons

Great attention must also be given to baffles. They are used to direct and control the flow of fluids within a simulation domain. When strategically positioned, they can influence flow behavior, evenly distribute fluid particles, and enhance the accuracy of simulations. Accurate use of baffles can contribute to obtaining more precise results, avoiding unwanted fluctuations or erratic flow behaviors. Baffles can be employed to reduce flow turbulence or create specific velocity profiles within the domain. This is valuable for simulating situations where turbulence needs to be minimized or controlled. Baffles can also simplify the mesh in certain regions of the domain, reducing computational load and accelerating simulations while

keeping precision in areas of interest. In many industrial applications, such as automotive or aerospace industries, baffles are used to model specific components or flow control devices, such as ducts, deflectors, or cooling systems.

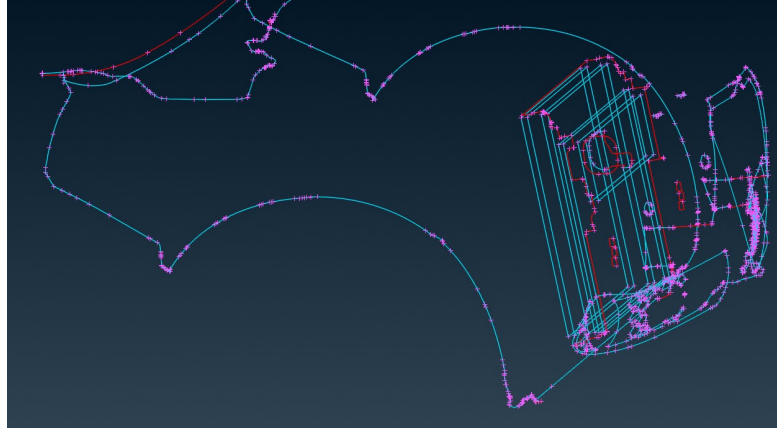


**Figure 5.2:** Example of Baffle in Stelvio: Heat Exchanger

## 5.2 Introduction of grooved tires

The first simulation involves the theoretical analysis of a vehicle equipped with an ideal slick tire. This slick tire undergoes a compression load of 18 mm on the front axle and 12 mm on the rear axle when the vehicle is placed in a specific configuration. The tunnel used for this simulation is set up in a standard configuration, with two different-sized mini belts mounted on the vehicle's axles. The front axle is equipped with mini belts measuring 410 X 265 mm, while the rear axle has mini belt measuring 410 X 340 mm. The tires mounted on the vehicle in this specific scenario are of size 235/65 R17, and these tires are used on both the front and rear axles of the vehicle.

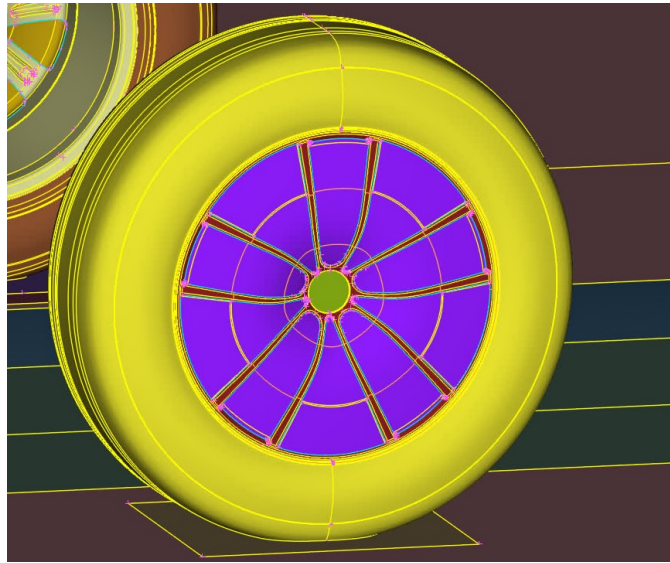


**Figure 5.3:** Slick tire

To obtain the aerodynamic coefficients  $C_x$  and  $C_z$  axle that can be compared with the results provided by the wind tunnel department, it is imperative to replicate the real tires within the simulation. These tires are the only simplified components that come into direct contact with the fluid flow. For simulating tire deformation, the chosen method involves surface morphing. This method entails having two surfaces: an initial one that replicates the shape of the undeformed tire and a final one that will be flattened in the contact area, having the same area as the previously taken imprint and retreating toward the wheel's center by an amount equivalent to the tire's compression under load. All elements situated between these two surfaces will be adapted to the geometry of the final, flattened surface.



**Figure 5.4:** Morphing tire

The obtained result, as shown in the figure, is a crucial phase in the process. The next step involves bringing the entire tire-rim-hub assembly to ground level to allow for the intersection of the tire with the surface of the Wind Simulation Unit (WSU). During this phase, a morphing of the vehicle's suspension will also be performed to adapt it to the new wheel center position. This means that the suspensions will need to be changed to enable proper interaction with the ground,

considering the new wheel positioning. This theoretical and practical approach is essential to ensure that the simulation accurately reflects real-world conditions and that the results obtained are valid for the vehicle's aerodynamic analysis.

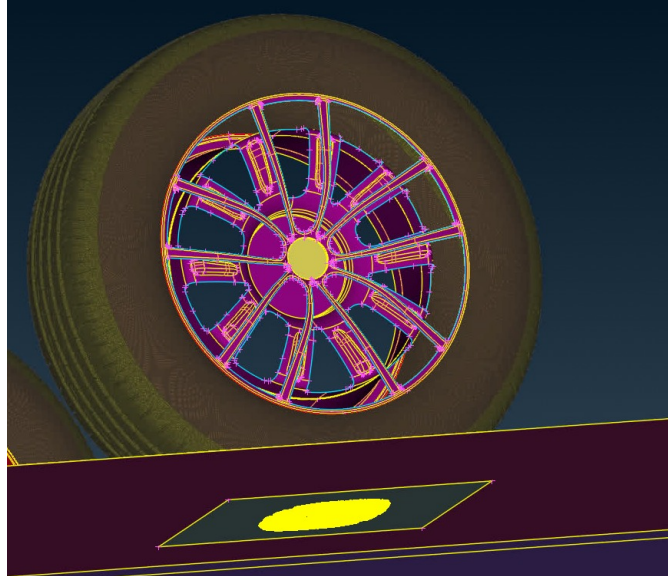


**Figure 5.5:** Grooved tire

### **5.3 Simulation of the various belt configurations**

Within the context of advanced aerodynamic analysis conducted within a wind tunnel, the first arrangement of conveyor belt systems holds paramount significance. Initially, these conveyor belt systems were strategically positioned centrally, being a typical starting point for a series of tests aimed at calculating the aerodynamic coefficients of a vehicle or specific configuration. This central arrangement serves as a fundamental reference for numerous experiments in the field of vehicle aerodynamics.

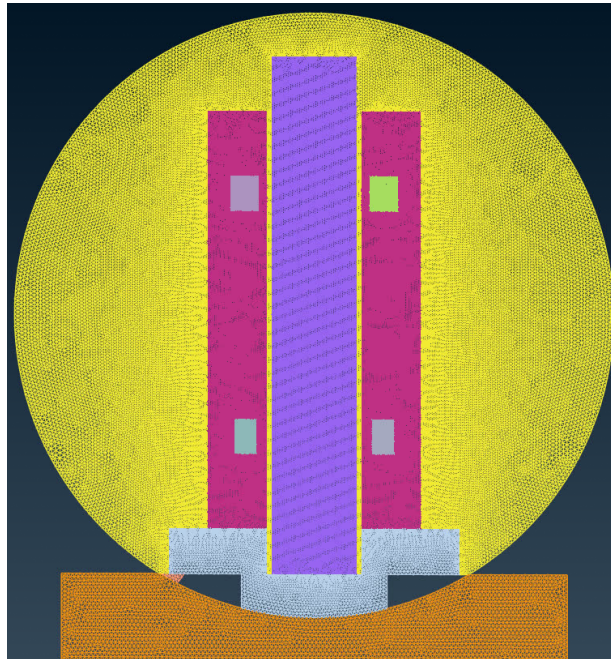


**Figure 5.6:** Belts in central position

Advanced analysis needs a comprehensive understanding of aerodynamic dynamics and their impact on the coefficients  $C_x$  and  $C_z$ . This understanding is achieved by examining in intricate detail how these coefficients vary in response to variations in the positions of the conveyor belt systems within the wind tunnel. For this reason, various configurations of conveyor belt system arrangements along a loop-shaped path within the wind tunnel were set up. Each of these configurations was specifically found through a Process Identification (PID) naming process, ensuring clear and unique categorization. The primary aim was to emulate the various arrangements experienced in real wind tunnels, thereby enabling the study of the effects of changes in the positions of the conveyor belt systems.

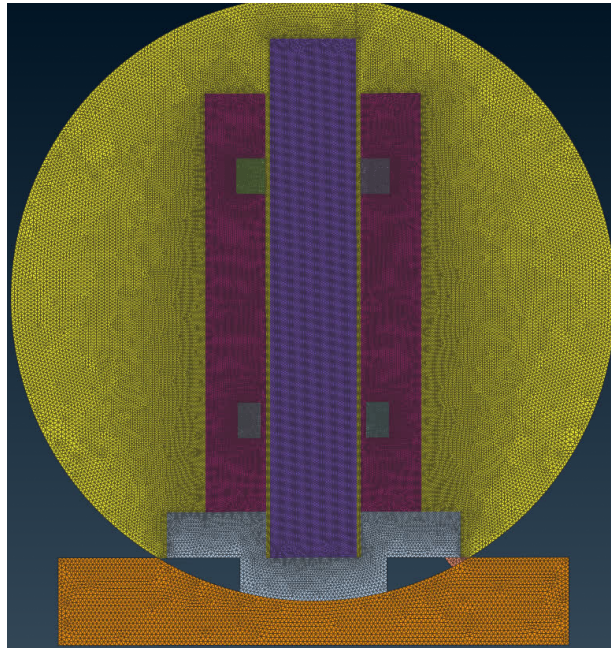


**Figure 5.7:** Example of possible belts configurations: maximum external position

It is important to underscore that, depending on the specific aims of the post-processing test, each of these configurations was granted the flexibility to introduce or exclude the variable of tire rolling speed. This approach enables a detailed analysis of tire kinematics in relation to the different conveyor belt system configurations, which in turn has an impact on the aerodynamic coefficients  $C_x$  and  $C_z$ .

## 5.4 Open FOAM

The first software used for CFD simulation is Open FOAM. It is a powerful and flexible development environment that enables engineers and researchers to solve a wide range of fluid-related problems, from computational fluid dynamics to heat transfer, combustion, pollutant dispersion, and much more. The simulation begins with the creation or import of a geometric model of the system to be analyzed. The geometry is then subdivided into a three-dimensional or two-dimensional grid of cells or finite elements. This grid, known as a mesh, is the domain in which the CFD calculations will be solved. To address the resolution of the problem in Computational Fluid Dynamics (CFD), it is essential to define boundary conditions. These conditions delineate how the fluid interacts with the surfaces within the study domain. These conditions, including inlet or outlet velocities, temperature, pressure, and others, play a crucial role in shaping the fluid dynamic behavior within the analyzed system. During this phase of development, the integration of information about the various conveyor belt system configurations in the simulation is also envisaged, as depicted in the reference illustration.

```
tunnel_WT_WF_belt_main
{
    U
    {
        type            tangentialVelocity;
        magnitude       38.89;
        direction        (1 0 0);
        value uniform   (38.89 0 0);
    }
}

tunnel_WT_WT_wheel-belt_FRT-LFT
{
    U
    {
        type            tangentialVelocity;
        magnitude       38.89;
        direction        (1 0 0);
        value uniform   (38.89 0 0);
    }
}
```

**Figure 5.8:** Belts configuration on Open Foam

This specific aspect is a fundamental part of the script, thus allowing for the modeling and detailed examination of variations in the positions of conveyor belt systems within the CFD context. Subsequently, the choice of the physical model to be used for the simulation is shown, which can range from laminar to turbulent flow problems, heat transfer, chemical reactions, and more. Open FOAM solves the Navier-Stokes equations to describe fluid behavior and is also capable of employing numerical methods, such as the finite volume method, to discretize and solve fluid equations. This entails iterating through the mesh domain in small time steps to calculate the fluid's behavior over time.

## 5.5 Results

### 5.5.1 Convergence of the simulations

In CFD simulation process, the control of residuals and convergence indicators plays a crucial role. These parameters supply a critical measure of the accuracy and reliability of the ongoing simulations. The analysis of residuals reflects the difference between the calculated and theoretical values, showing the degree of accuracy of the obtained results. A careful control of these parameters is crucial to ensure that the simulation is effectively capturing the desired physical behaviors of the system under examination. If the results show an acceptable level of convergence, and the residuals are within predetermined limits, one can go ahead with the detailed analysis of the pressure field. However, if the results do not meet the desired convergence criteria, it becomes essential to adopt proper corrective actions. These actions may include increasing the number of iterations to allow the process to converge towards a stable solution or changing the physical model used to better represent the real behavior of the system.

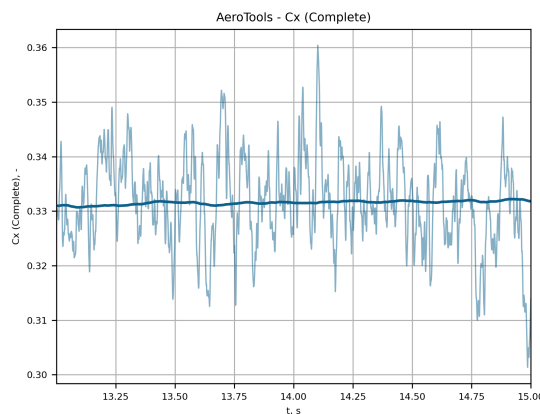


**Figure 5.9:** Convergence in Cx simulation

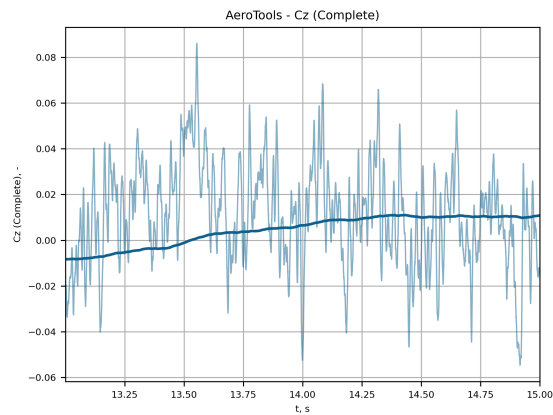


**Figure 5.10:** Convergence in Cz simulation

The images show how, after a certain number of iterations, especially in this case for Cz, convergence is achieved. It is important to underline that the coefficients displayed are not the only relevant indicators to see, but they certainly play a significant role in ensuring a correct simulation. It is important to note that, although the analysis of residuals and convergence indicators is fundamental, there are also other critical indicators to consider ensuring right and reliable simulation. A thorough understanding of these parameters and their careful management can significantly contribute to improving the overall quality of CFD simulations.

### 5.5.2 Transversal moving 17” wheels case

In the simulations, the behavior of the aerodynamic coefficients was analyzed as the position of the belts was varied. This investigation was conducted by adjusting both the front and rear belts individually, as well as altering both simultaneously. During various analyses, the reference configuration is established based on the results obtained using both **belts in the central position and with cup-less tires**. An example of this approach is highlighted in the attached images, which represent all the configurations of the rear belts.

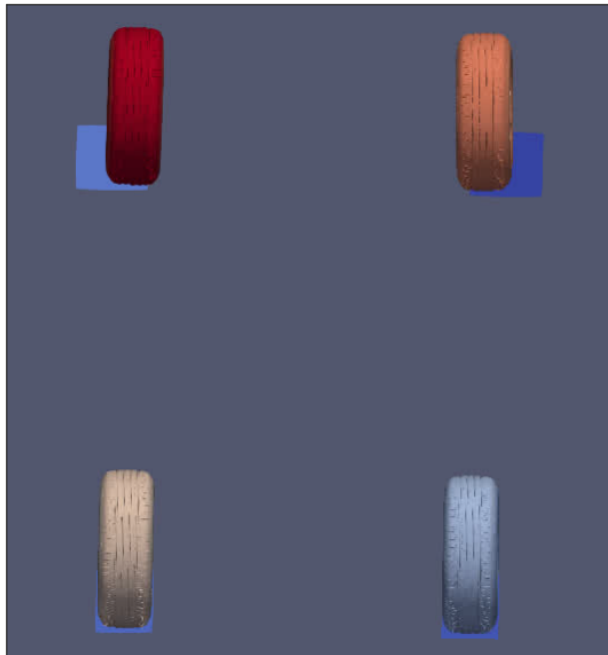


**Figure 5.11:** Rear belts in external configurations

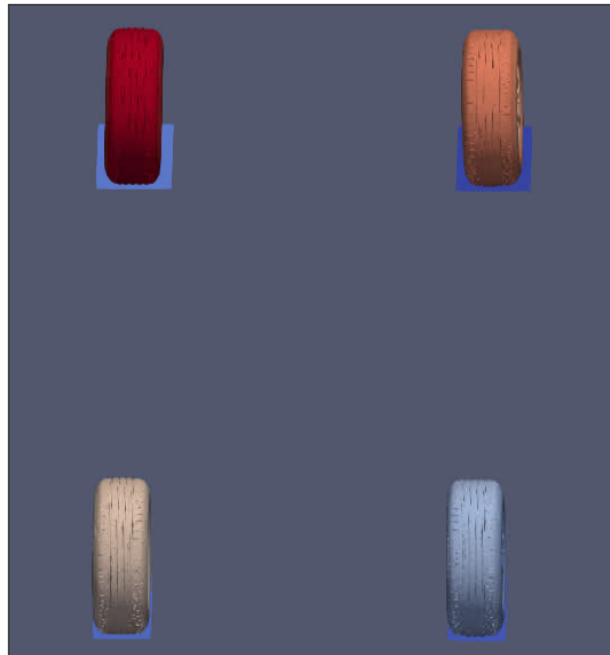


**Figure 5.12:** Rear belts in central configuration

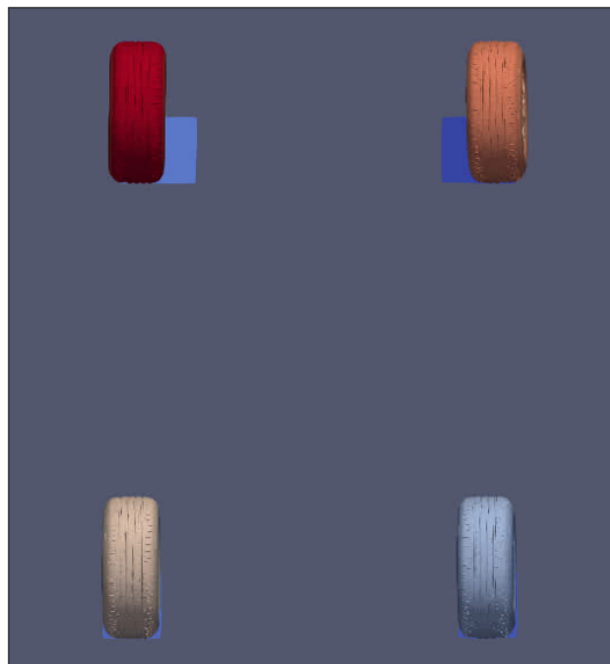


**Figure 5.13:** Rear belts in internal configurations

### Cx Observations

From the CFD simulations, it has appeared that the optimal configuration for reducing the aerodynamic coefficient  $C_x$  is achieved through the manipulation of the positions of both the front and rear belts, with the belts positioned centrally. A detailed analysis of the data presented in the attached image of the deltas highlights a trend in the change of  $C_x$  that contradicts the movement of the positions of the front and rear belts.

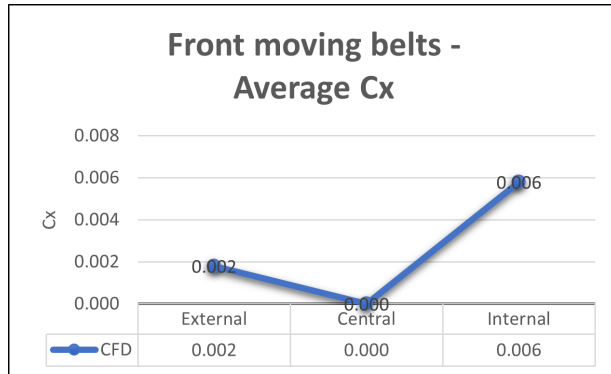


**Figure 5.14:** Average  $C_x$  during front moving belts

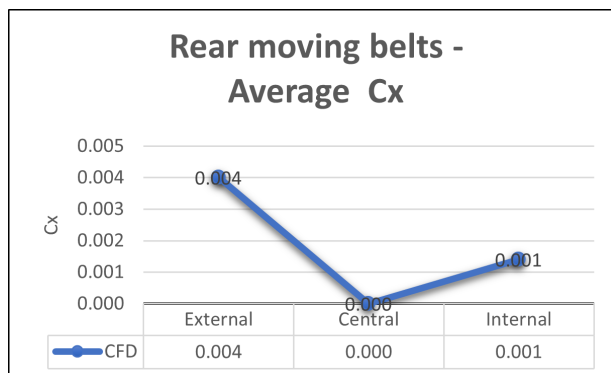


**Figure 5.15:** Average  $C_x$  during rear moving belts

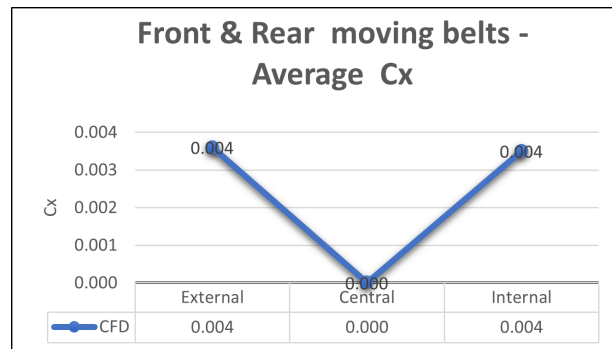


**Figure 5.16:** Average Cx during front and rear moving belts

A significant increase in the delta value compared to the central configuration was notably seen when the position of the front belts was altered, particularly within the configuration of the belts themselves. This marked variation suggests a high sensitivity of the aerodynamic system to changes in the arrangement of the front belts. The trend of the variation of the aerodynamic coefficient  $C_x$ , when moving the positions of the rear and front belts, is completely opposite, as clearly highlighted in the attached images of the deltas. This phenomenon was further emphasized through an analysis of the velocity graph, which revealed the presence of regions with heightened turbulence, notably concentrated in the vicinity of the right tire.

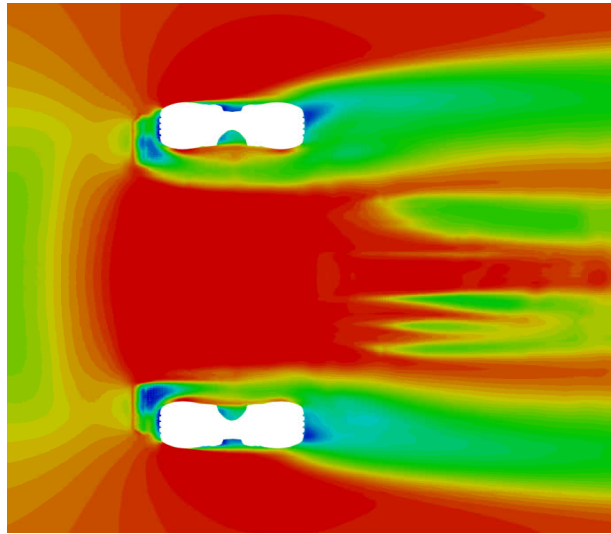


**Figure 5.17:** Velocity of front tires in Front belts central configuration

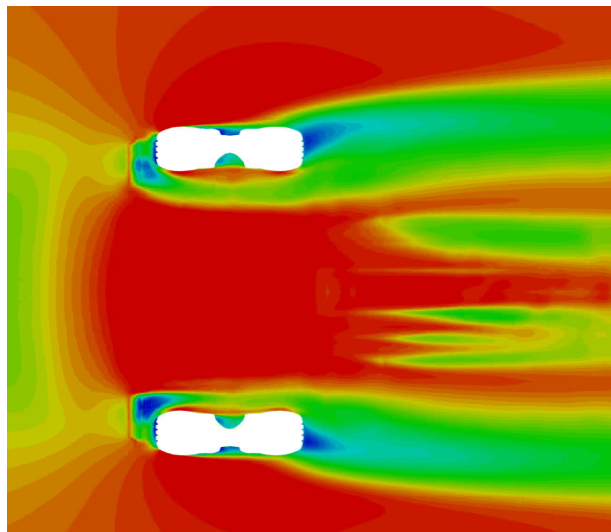


**Figure 5.18:** Velocity of front tires in Front belts internal configuration

This observation shows a complex interaction between the position of the front belts and the dynamics of the aerodynamic flow, highlighting potential areas for further optimization to enhance overall aerodynamic performance. Finally, by simultaneously shifting the belts to their maximum outward and inward configurations, the delta value remains the same compared to the central configuration, as evidenced in the attached image.

### Cz Observations

Through complex simulations of the aerodynamic coefficient  $C_z$ , an interesting phenomenon has appeared: an opposite trend has been highlighted during the displacement of the front and rear belts, a pattern that recalls what was seen for the  $C_x$  coefficient.

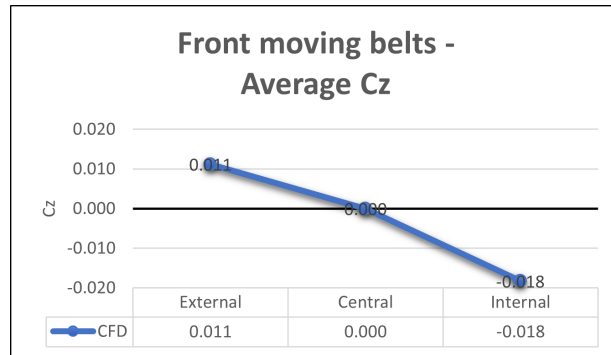


**Figure 5.19:** Average  $C_z$  during front moving belts

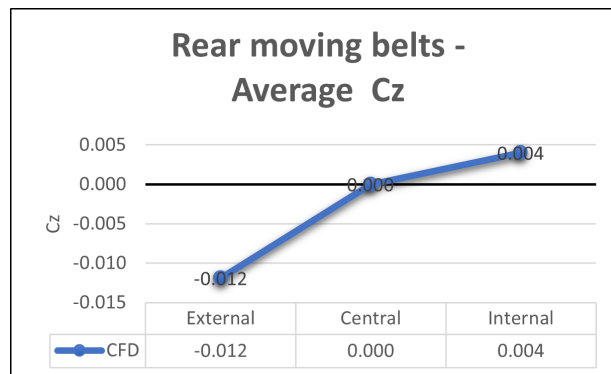


**Figure 5.20:** Average  $C_z$  during rear moving belts

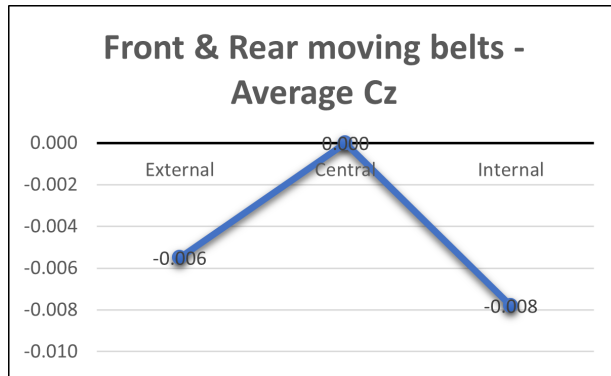


**Figure 5.21:** Average Cz during front and rear moving belts

Taking a closer look at the behavior of  $C_{za}$  on the front wheels, is noticed that when the front belts are moved,  $C_z$  faithfully followed the overall trend. However, this scenario did not repeat itself when are changes to the positions of the rear belts. On the contrary, the reduction in the  $C_{za}$  was clearly visible when the belts were moved from their central position, as indicated in the attached images.

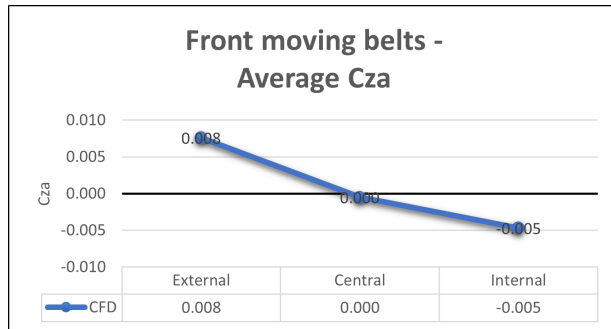


**Figure 5.22:** Average  $C_{za}$  during front moving belts

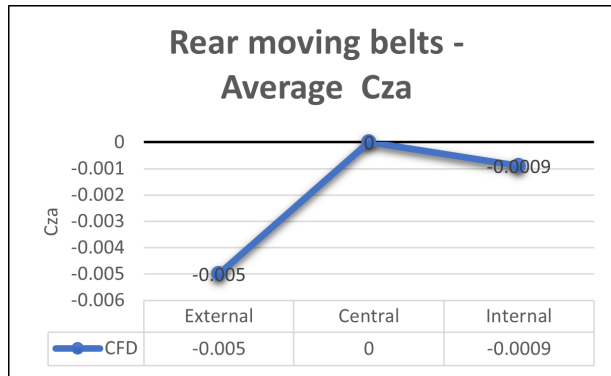


**Figure 5.23:** Average Cza during rear moving belts

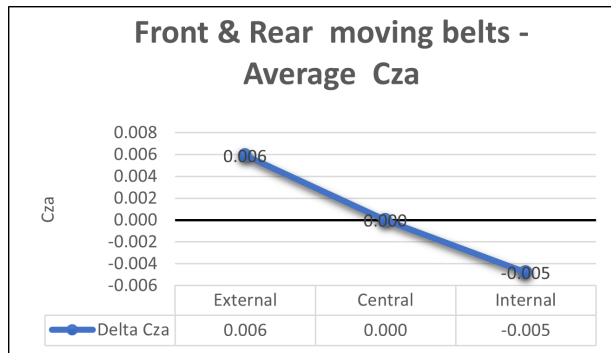


**Figure 5.24:** Average Cza during front and rear moving belts

Regarding the  $C_{zp}$ , an interesting behavior has emerged. In both the displacement of the front belts and the displacement of the rear belts, we noticed a similar trend between  $C_z$  and  $C_{zp}$ , as shown for example in this image.

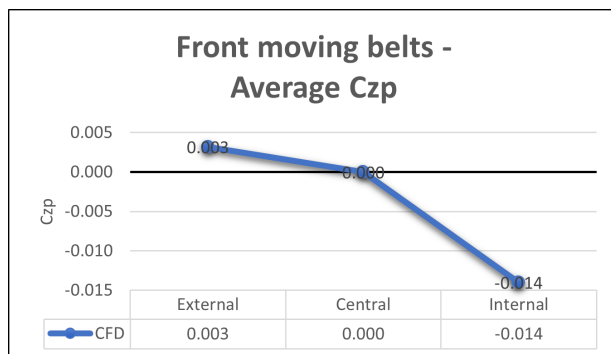


**Figure 5.25:** Average  $C_{zp}$  during front moving belts

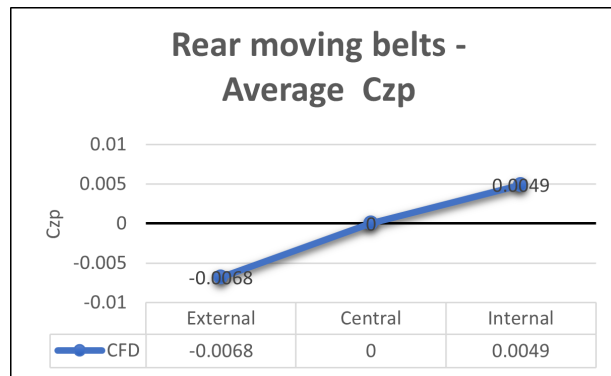


**Figure 5.26:** Average  $C_{zp}$  during rear moving belts

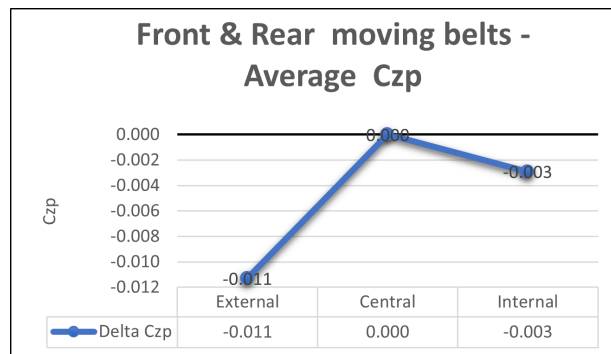


**Figure 5.27:** Average  $C_{zp}$  during front and rear moving belts

In this case as well, the only exception occurs when both belts are moved simultaneously: this action results in an overall reduction of  $C_z$ . As in the two previously mentioned cases, a similar trend is seen for  $C_{zp}$ . From a more comprehensive analysis, the displacement of the belts significantly affects their respective  $C_z$  coefficient, as proved in the images below, where the movement of the front belts generates a greater delta in  $C_z$ ; the same applies when the rear belts are moved.

### 5.5.3 Wheel cover case

To prove how the addition of fairings leads to a decrease in the aerodynamic coefficient  $C_x$  in CFD simulations, the CAD model of the S2A Fairing was employed. The S2A fairing features a slightly more convex profile compared to the one used for wind tunnel simulations for the Stelvio, namely the FSWT. The simulations were conducted by manipulating the position of the front belts, as earlier analyses revealed a significant deviation in the coefficient of aerodynamic resistance ( $C_x$ )

when the belt configuration was varied with respect to the central reference position. From the analysis of the  $C_x$  trend illustrated in the figure below, a significant variation is seen. Specifically, the configuration characterized by the minimum  $C_x$  is found when the belts are in their outer position. Conversely, moving towards the inner configuration results in an increase in  $C_x$ . This reversal of the trend can be primarily attributed to the fact that both the outer and inner configurations, with the addition of the cups, led to a reduction in  $C_x$  by just over 2 thousandths, while the central configuration did not experience significant effects from the addition of the cups.

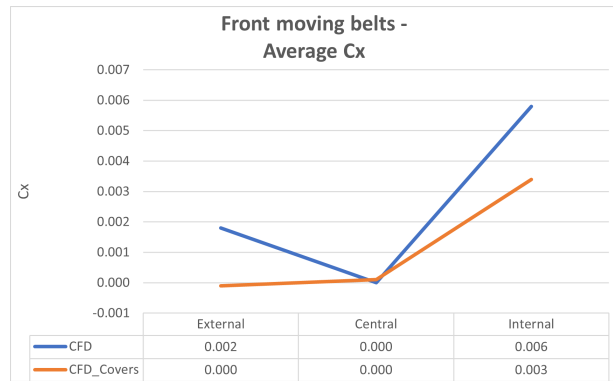


**Figure 5.28:** Average  $C_x$  during front moving belts with covered wheels

A similar behavior was seen for the lateral lift coefficient ( $C_{za}$ ), confirming previous results obtained without the addition of cups. In contrast, a completely different dynamic was found for the vertical lift coefficient ( $C_{zp}$ ). Moving from the central configuration to the outer one, the vertical lift coefficient shows an increase rather than a decrease.

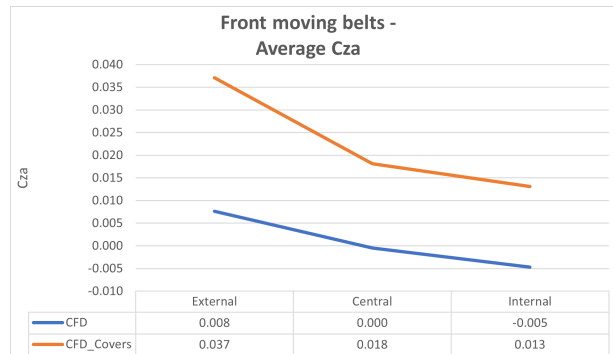


**Figure 5.29:** Average  $C_{za}$  during front moving belts with covered wheels

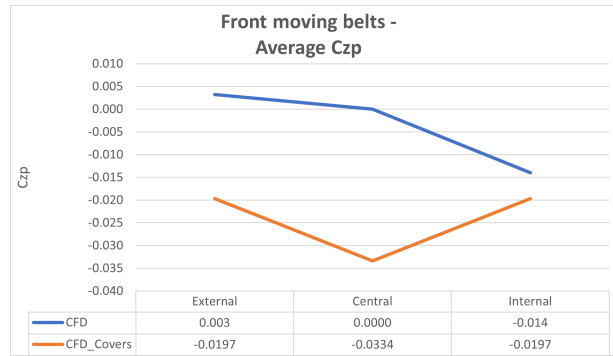


**Figure 5.30:** Average  $C_{zp}$  during front moving belts with covered wheels

The same behavior observed in the case of the front deflectors is noticeable when analyzing the movements of the front belts. Although, in this case as well, the presence of the cups has led to a significant reduction in the drag coefficient for the external configuration, the lower  $C_x$  is achieved with the central configuration. As can be seen in the image, however, the difference with the other two configurations is about one thousandth.



**Figure 5.31:** Average  $C_x$  during rear moving belts with covered wheels

Examining the components of the lift coefficient, it can be noted, as seen in the front deflector simulation, the same trend in  $C_{za}$ . In this case, the delta value between the external and central configurations is much smaller. Also, in this case, as in the previous one, the same trend is not observed between simulations with and without cups for  $C_{zp}$  coefficient. While moving the configuration of the front belts showed an opposite trend when shifting from the central to the internal configuration, for the rear belt simulations, this discrepancy is observed when moving the belts from the central to the external configuration.



**Figure 5.32:** Average Cza during rear moving belts with covered wheels



**Figure 5.33:** Average Czp during rear moving belts with covered wheels

## 5.6 Field Pressure

The grid is a fundamental element in CFD simulation, as it divides the study domain into a series of discrete elements. It allows the CFD software to numerically solve the complex equations of fluid dynamics. The obtained results include physical parameters such as pressure, velocity, and temperature within the simulated domain. One of the key considerations in creating the mesh is domain resolution, that is, the density of elements within the mesh itself. A finer mesh, with more elements, supplies a more detailed simulation but entails an increase in computational time. This has been implemented in the areas of the belts closest to the Tires.

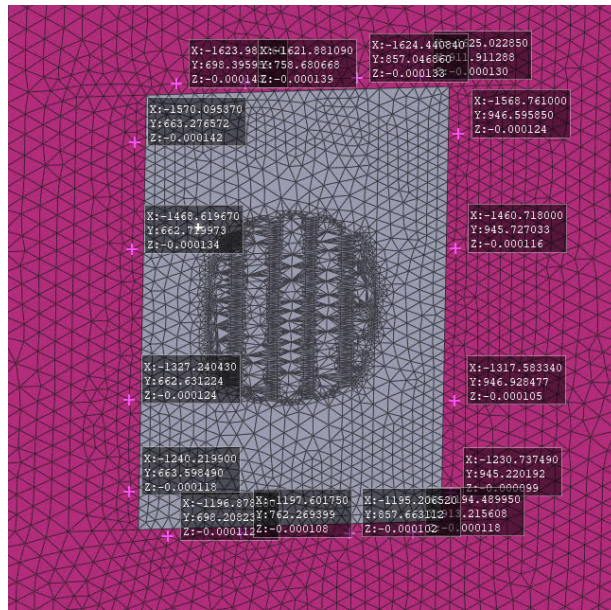


Figure 5.34: Coordinates of the points around the belt

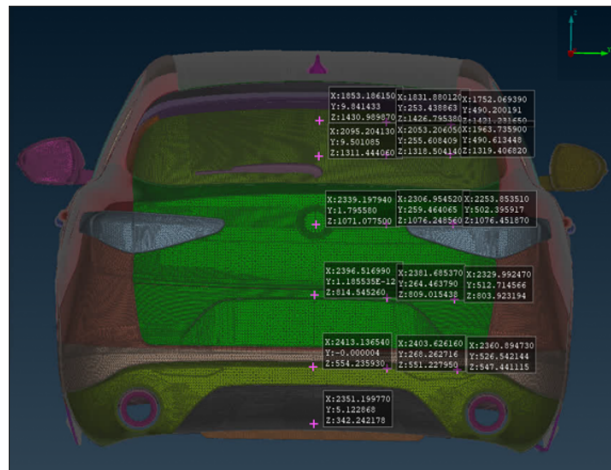
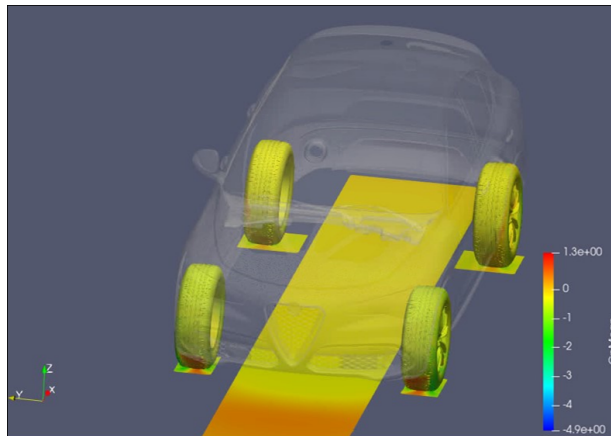


Figure 5.35: Coordinates of the points in the back

The image shows an example of selecting equidistant points. Through scripts on Open FOAM, during post-processing, it will be possible to obtain the value of the field pressure. A denser mesh can also be seen in areas where greater accuracy is needed, such as around complex objects, and less dense in other areas where lower resolution is sufficient. This allows for the optimization of the use of computational resources.



**Figure 5.36:** Field pressure of tire and belts

### Cx considerations

The aerodynamic coefficient  $C_x$ , which is the aerodynamic resistance of an object in an airflow, can vary in response to changes in the pressure coefficient  $C_p$ . However, the precise relationship between  $C_x$  and  $C_p$  depends on several factors, such as the shape and size of the object, flow conditions, and specific characteristics of the aerodynamics of the system under consideration. Generally, when the pressure coefficient  $C_p$  increases, the aerodynamic resistance represented by  $C_x$  also tends to increase. Conversely, when the pressure coefficient  $C_p$  decreases, the aerodynamic resistance  $C_x$  tends to decrease. This relationship may vary depending on the specific context and study conditions, so there may be exceptions to this general relationship.

From the analysis conducted at the back, the most significant differences compared to the central belt configuration are observed when the front belts are moved. As can be seen from the image, there are areas with higher  $C_p$ , thereby proving, as previously observed, how the increase in  $C_x$  in these two cases is also attributed to this factor.

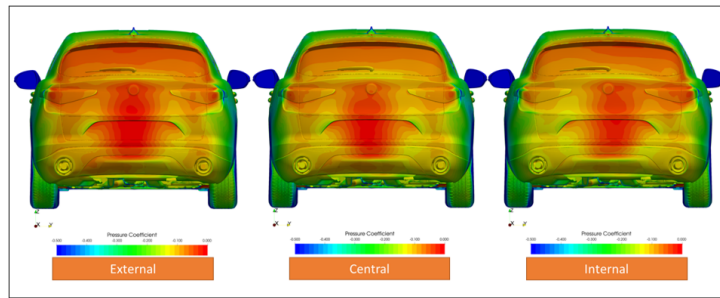


**Figure 5.37:** Cp back comparisons moving the front belts

Under a more detailed analysis, this trend is also visible through the values of the Cp obtained punctually at the 16 different points on the back of the vehicle. We can see how the movement of the belts has generated a general increase in the Cp.

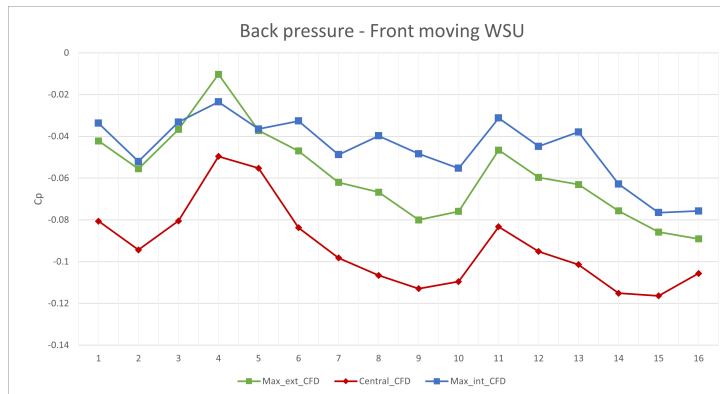


**Figure 5.38:** Cp back coefficients during front moving belts

Conversely, there appear to be no significant differences in Cp when rear belts are moved.

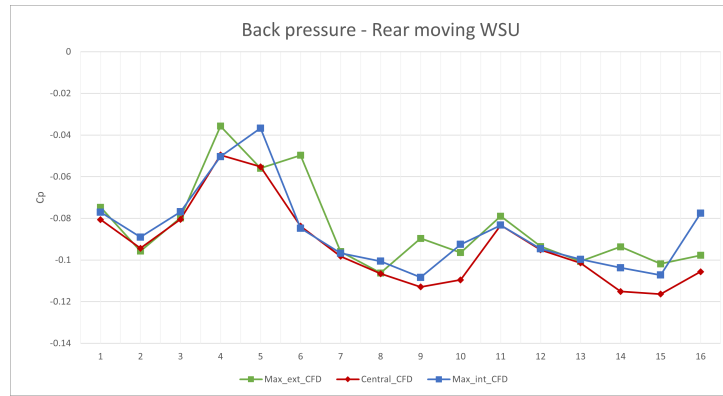


**Figure 5.39:** Cp back coefficients during rear moving belts

The trend stays unclear in the case where both the rear and front belts are moved, despite no persistent difference being observed among the three scenarios, as depicted in the image.

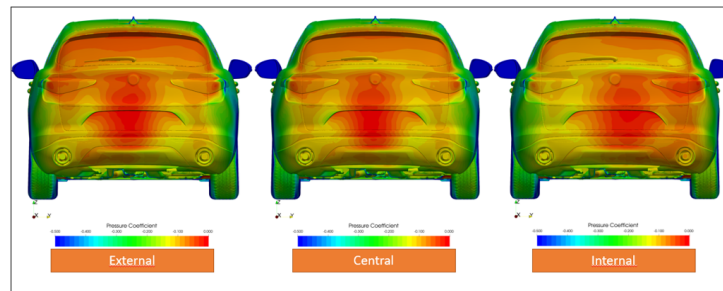


**Figure 5.40:** Cp back coefficients during front and rear moving belts

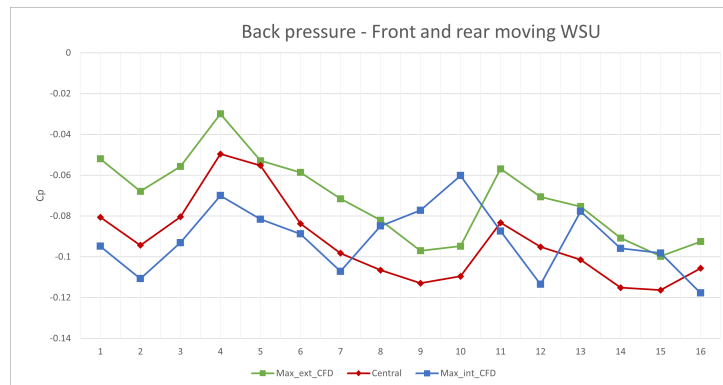


**Figure 5.41:** Cp back coefficients during front and rear moving belts

### Cz considerations

From an aerodynamic perspective, the same correlation between the pressure coefficient ( $C_p$ ) and the aerodynamic resistance coefficient ( $C_x$ ) is also present between  $C_p$  and the lateral aerodynamic coefficient  $C_z$ .

As evidenced by the images obtained through post-processing in Paraview, it is evident that the faithful reproduction of the field is accurate: in the case of the inner belt, the external sensors, located near the shoulder of the wheel, detect a peak of negative pressure (green intakes 1-2-3 ) caused by a strong pressure gradient. On the other hand, in the case of the completely outer belt, it is the internal sensors that perceive the presence of the vortex near the tire. However, if the peak of negative pressure is detected by the sensors, this suggests that it is outside the WSU carpet. Consequently, the load cells do not sense it, causing an increase in the value of  $C_z$ . This explains the increase in  $C_{za}$  by moving the belt outward. This trend is confirmed by the progressive increase in the light green bars in the previous graphs.

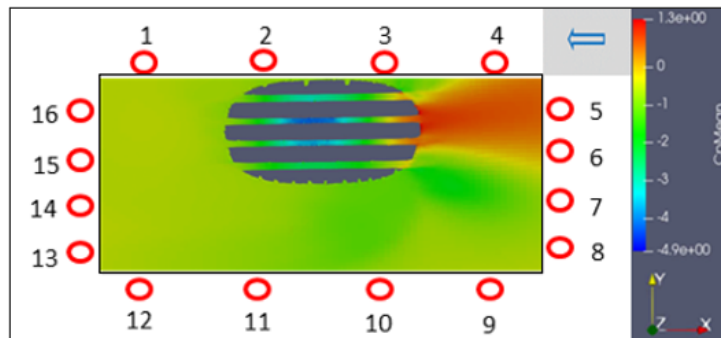


**Figure 5.42:** Field pressure of the front right belts in external configurations

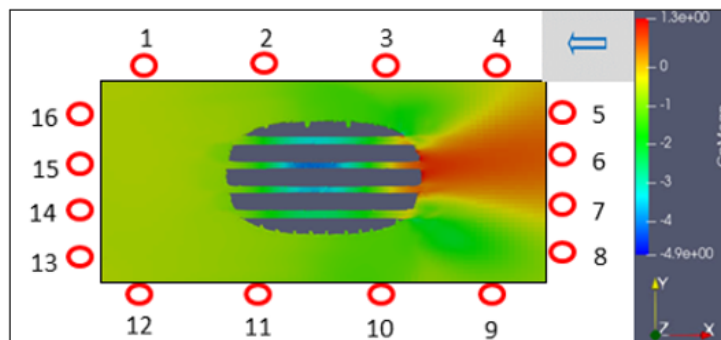


**Figure 5.43:** Field pressure of the front right belts in central configurations

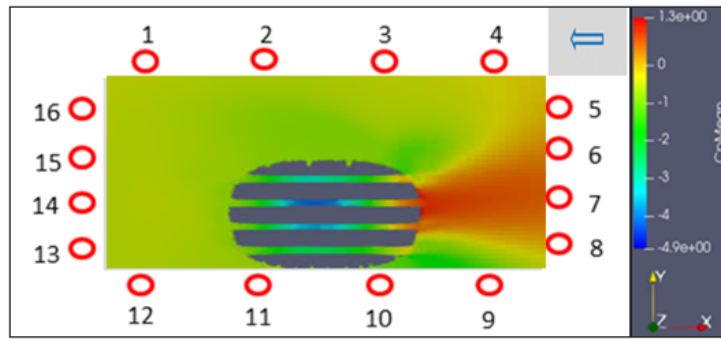


**Figure 5.44:** Field pressure of the front right belts in internal configurations

This result is also confirmed by the Excel graphs illustrating the values of the pressure coefficient derived through the previously described process.

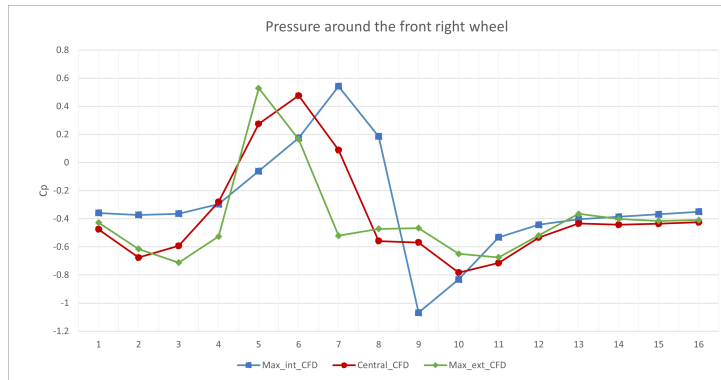


**Figure 5.45:** Front right average Cp during moving front belts

Furthermore, it can be seen that the movement of the belts from the outer configuration to the inner one has caused the displacement of a positive peak of Cp for each swap, as demonstrated in the corresponding graph. There is no variation in the pressure coefficients in the case where both the rear and front belts are moved, compared to the case where only the front belts are moved. The same trend can be seen when the rear belts are moved. As can be seen, green areas are close to points 10-11-12 for the external configuration, while they are near points 2-3-4 for the internal one.

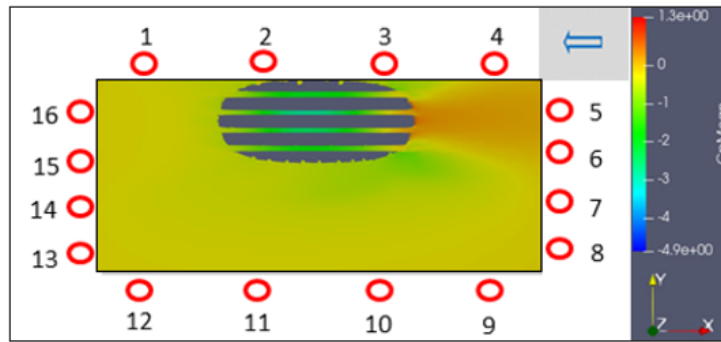


**Figure 5.46:** Field pressure of the rear right belts in external configurations

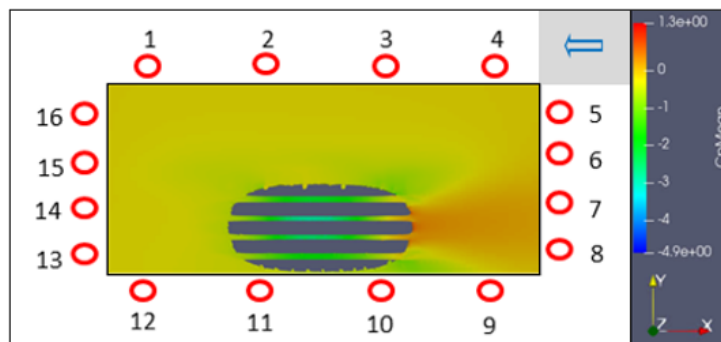


**Figure 5.47:** Field pressure of the rear right belts in internal configurations

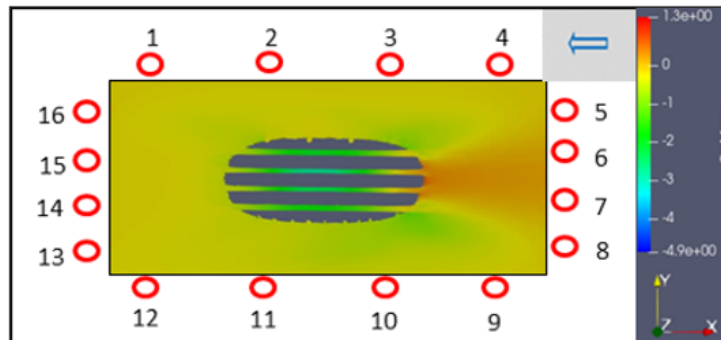


**Figure 5.48:** Field pressure of the rear right belts in internal configurations

The pressure distribution behind the tire is also represented in the graph at the rear for clarification.

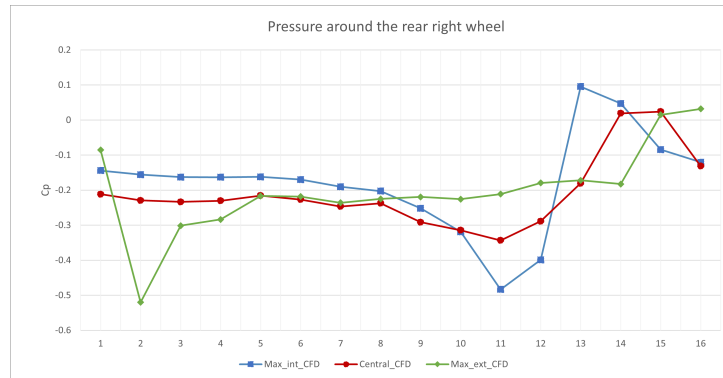


**Figure 5.49:** Rear right average Cp during moving rear belts

However, no variation in the pressure coefficient ( $c_p$ ) is observed for the various belts in the case where the opposite belts are moved, as seen in the attached images.

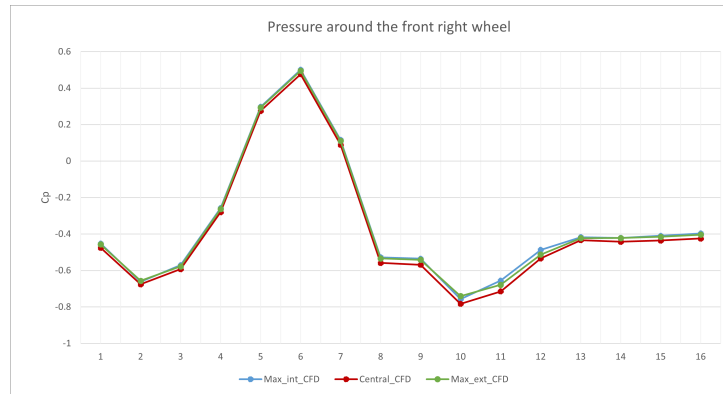


**Figure 5.50:** Front right average Cp during moving rear belts

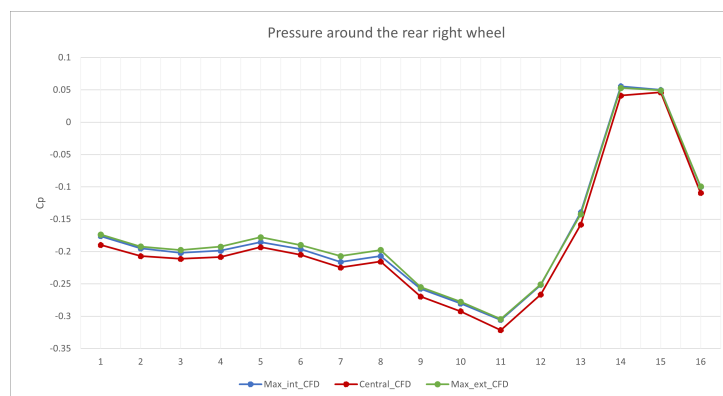


**Figure 5.51:** Rear right average Cp during moving front belts

## Chapter 6

# CFD and WT comparison

Two different approaches have been adopted to study the same phenomena to compare the results and finding the best correlation between the two methods, helping future possible studies.

### 6.1 Wind tunnel test

The experimental evaluation of the aerodynamic coefficients was conducted using the aerodynamic Wind Tunnel found in Orbassano. The tests were divided into two main sessions. The first session focused on visualizing the aerodynamic forces while varying the relative position between the wheels and the Wheel Suspension Unit (WSU). It's worth noting that only the mini belts under the wheels were adjusted according to the different configurations to analyze, as the vehicle remained fixed to the ground.



**Figure 6.1:** Central position between front wheels and WSU



**Figure 6.2:** Limit condition between wheel and WSU

As a second step, pressure fields were analyzed to compare the analyses conducted between CFD and WT. A piece of cardboard was used to facilitate the movement of the WSU for each configuration.

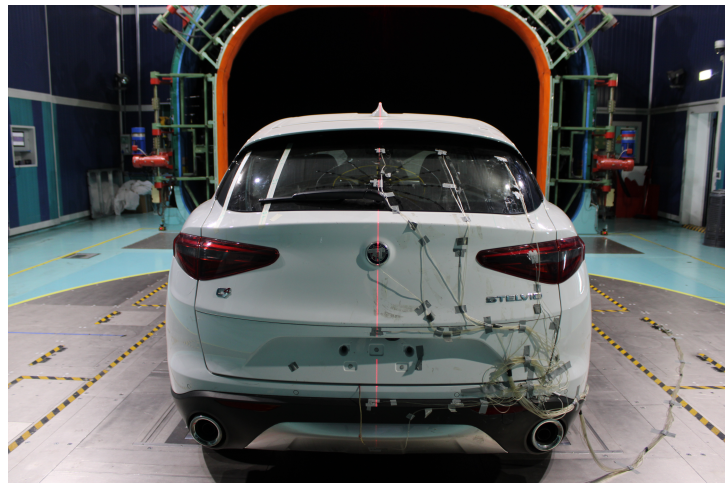


**Figure 6.3:** Position sensors on the rear car



Figure 6.4: Position sensors around the wheel

## 6.2 Aerodynamic coefficients

### 6.2.1 $C_x$ Correlation

From the evaluation of the data presented in the images below, detailing the values of the coefficients of aerodynamic resistance ( $C_x$ ) derived from computational fluid dynamics (CFD) simulations and wind tunnel tests, a notable alignment between the two methodological approaches appears. The slight difference of 10 hundredths of a unit falls within an acceptable range, indicating substantial congruence between the results obtained from the two methods.

CONFIGUARTIONS		$C_{x_{WT}} - C_{x_{CFD}}$
	ext	-0.011
FRONT moving WSU	central	-0.008
	int	-0.012
	ext	-0.013
REAR moving WSU	central	-0.008
	int	<b>-0.001</b>

Table 6.1: Delta  $C_x$  correlation

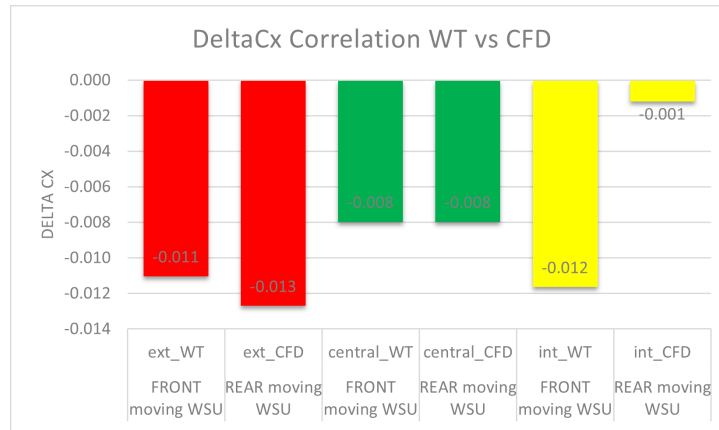


**Figure 6.5:** Delta Cx correlation

However, to achieve a more precise correlation, it is advisable to consider perfecting data coherence, which could be influenced by variables such as the quality of the grid used, and the level of approximation adopted in simulating the dynamics of rotating wheels. These parameters could introduce significant distortions within the scope of the study in question. Analyzing the trends of Cx by manipulating the belt positions in various configurations reveals a slight discrepancy between the outcomes of the two methods. In the case of CFD simulations, shifting the front belts first and the rear ones after results in the configuration with the belts placed centrally as the best choice in terms of Cx.

Conversely, in the wind tunnel experiments, the most effective configuration in terms of Cx involves placing the belts in their outer configuration in both cases. It is precisely in this configuration that the greatest disparity between the CFD results and the findings from the wind tunnel tests is seen. To address this divergence, two potential enhancements could be considered: improving the quality of the grid or implementing a wheel cover to mitigate the issues in that specific area.

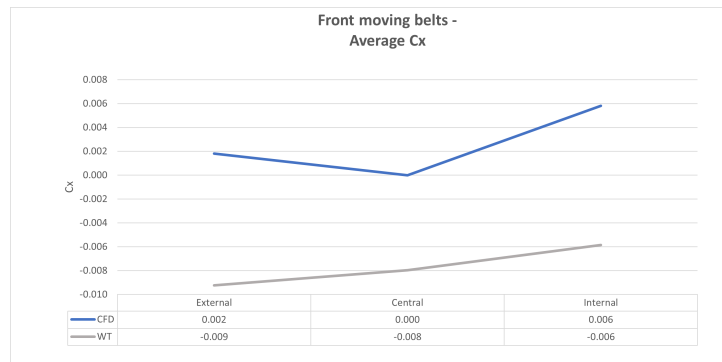


Figure 6.6: Cx trend comparison - Front Wsu

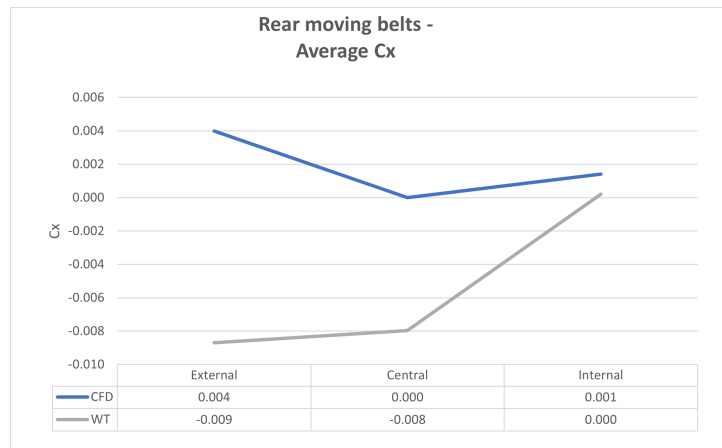


Figure 6.7: Cx trend comparison - Rear Wsu

Next sections will present the results of simulations with the wheel cover.

### 6.2.2 Cz correlation

Conducting a comparative analysis of the vertical force coefficient ( $C_z$ ) between simulations for the  $C_x$ ,  $C_{za}$ , and  $C_{zp}$  cases, it is clear at first glance that there is a lack of numerical correlation between the two simulations. However, this disparity is not considered a significant issue as the thesis's aim is to analyze the trends seen in the various conducted exercises. Specifically, examining the general  $C_z$  trend when the front flaps are displaced, a similar trend between the CFD simulation and the Wind Tunnel (WT) simulation can be noted. It is noteworthy that the reduction in value from the central configuration to the internal one is more pronounced in the CFD simulation. Likewise, the trend stays identical when

the rear flaps are shifted. In both simulations, the greatest delta is seen when transitioning from the central configuration to the external one.

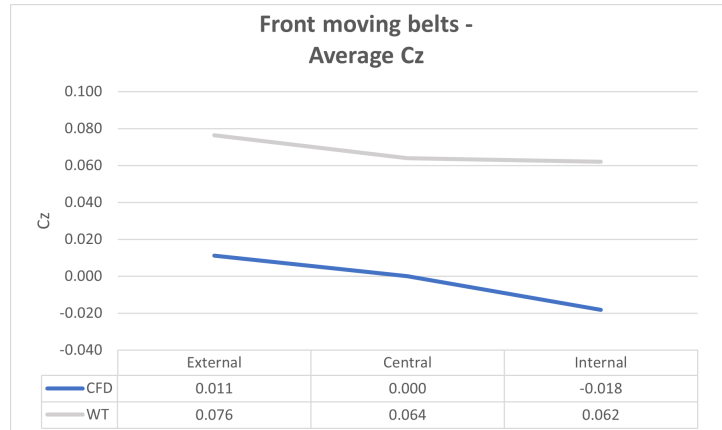


**Figure 6.8:** Cz trend comparison - Front Wsu



**Figure 6.9:** Cz trend comparison - Rear Wsu

However, a more detailed analysis of the two components of  $C_z$  highlights a discrepancy between the findings from the analyses of the front  $C_{za}$  and the rear  $C_{zp}$ . While both methods show the same trend for the front coefficient  $C_{za}$ , supplying significant correlation for understanding the phenomenon and valuable data for potential future studies, the same cannot be said for  $C_{zp}$ .

When the front belts are displaced, an entirely opposite trend is seen between the two simulations. However, shifting the configuration of the rear belts generates

a distinct difference between the CFD and WT simulations in the external configuration, a characteristic that was previously seen and highlighted in the CX paragraph.

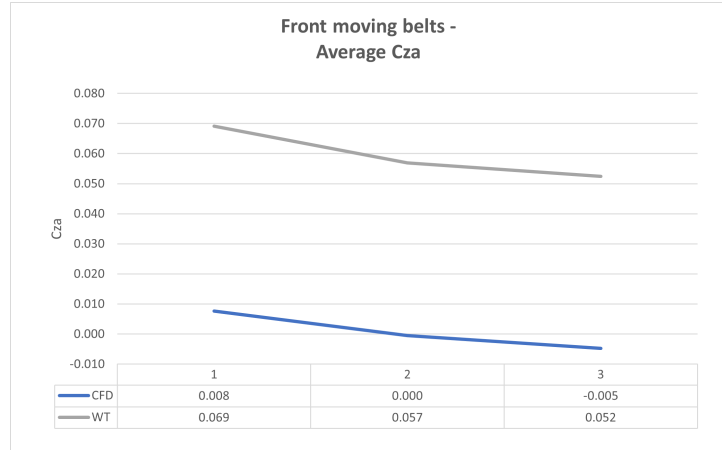


**Figure 6.10:** Cza trend comparison - Front Wsu

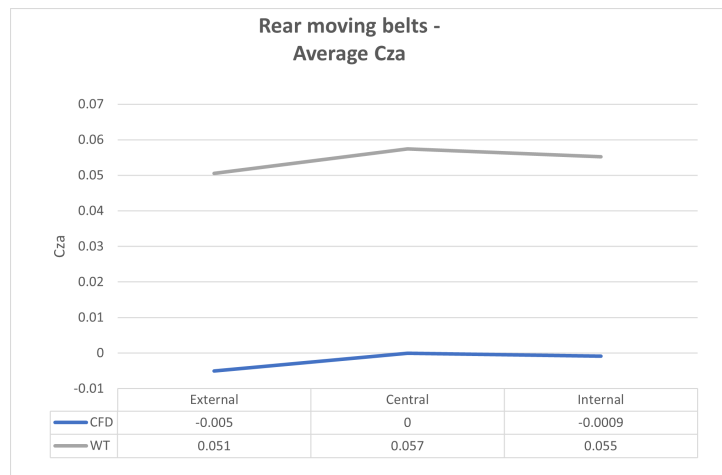


**Figure 6.11:** Cza trend comparison - Rear Wsu

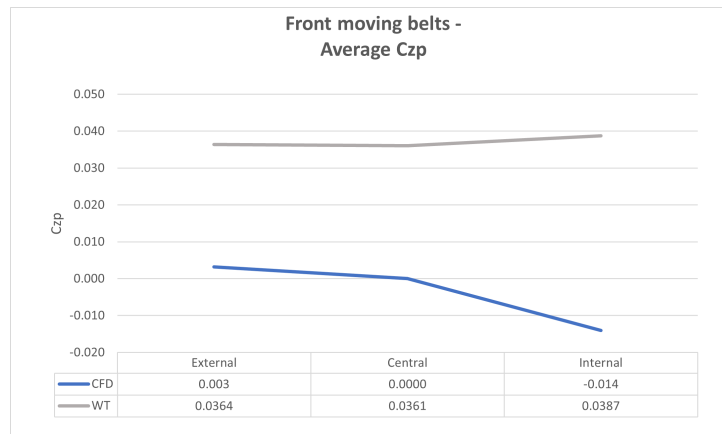


**Figure 6.12:** Czp trend comparison - Front Wsu



**Figure 6.13:** Czp trend comparison - Rear Wsu

Regarding the CX coefficient, to improve its simulation, one could consider adopting a higher quality grid or using a wheel cover. However, it has historically been challenging to find the best correlation in simulating aerodynamic coefficients, as proved by past numerical studies. Therefore, to confirm that the phenomena discussed in this thesis have the same impact on both methods, analyses of the pressure coefficients have been conducted, and their conclusions will be discussed in the upcoming sections.

### Cx-Cz correlation improvement

The incorporation of cups has brought about significant improvements in the level of agreement between CFD and wind tunnel simulations in the simulated cases. From the initial analysis conducted on the simulations of the frontal moving belts, for the case without cups, a disparity in the  $C_x$  trend was observed when transitioning from the outer to the central configuration of the front belts. However, with the addition of cups, this characteristic discrepancy vanished entirely. In both cases, an increasing trend in  $C_x$  is noticeable when transitioning from the outer to the inner configuration. Examination of the rear belts, in simulations with cups, reveals an almost linear trend in the drag coefficient. The significant delta observed in the case without cups, transitioning from the external to the central configuration, is absent here. Similarly, the substantial delta observed in wind tunnel simulations, transitioning from the central to the internal configuration, is not evident in this analysis.

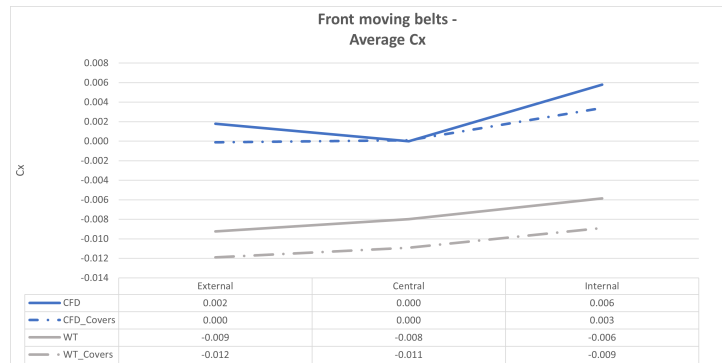


**Figure 6.14:** Comparison CFD and WT  $C_x$  average during front moving belts with covered wheels



**Figure 6.15:** Comparison CFD and WT Cx average during reae moving belts with covered wheels

It is noteworthy that a similar trend between CFD and WT, for both cases, is also seen for Cza and Czp thanks to the use of covers. While, for the simulations done on the front belts, the decreasing trend when transitioning from the outer to the inner configuration had already been found for the former case, even in simulations without cups, for Czp, as previously observed, this characteristic was absent without cups. In this instance, for both simulations, the case with the lowest Czp corresponds to the one with the front and rear belts in the central configuration.

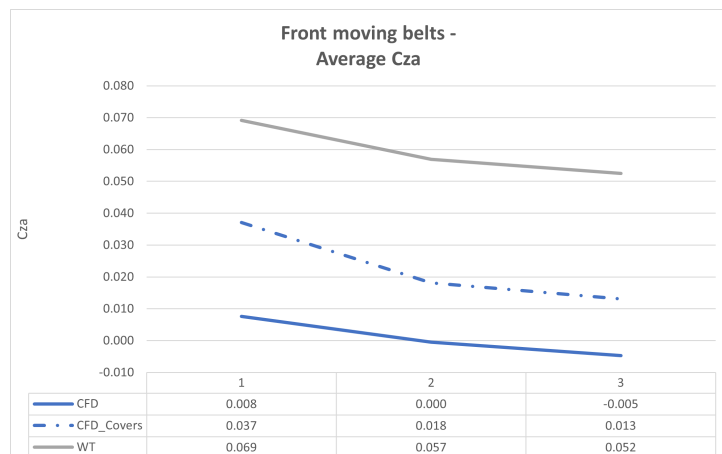


**Figure 6.16:** Comparison CFD and WT Cza average during front moving belts with covered wheels

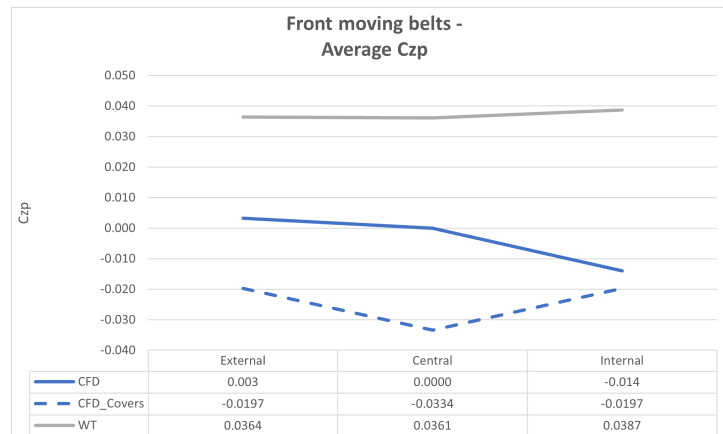


**Figure 6.17:** Comparison CFD and WT  $C_{zp}$  average during front moving belts with covered wheels

The same conclusions can be drawn from the analysis of the movements of the rear belt configurations. Here, too, the same trend for  $C_{za}$  between simulations with covers in CFD and the Wind Tunnel is evident, a characteristic already present in simulations without their use. It is in the analysis of  $C_{zp}$  that the improvement in similarity between WT and CFD becomes noticeable. The use of covers has made the trends between CFD and WT very similar, although the delta between the extreme configurations and the central one is more pronounced in the CFD simulation.

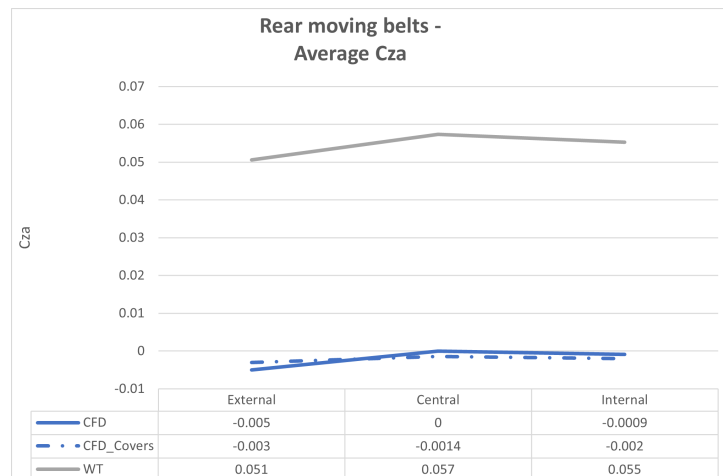


**Figure 6.18:** Comparison CFD and WT  $C_{za}$  average during rear moving belts with covered wheels

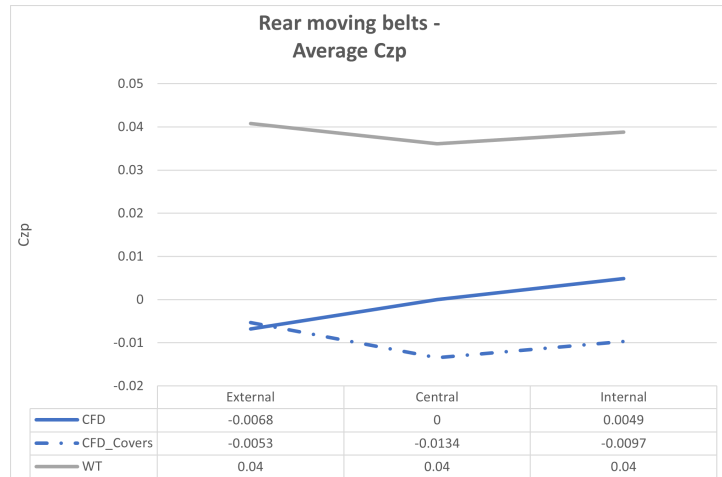


**Figure 6.19:** Comparison CFD and WT  $C_{zp}$  average during rear moving belts with covered wheels

### 6.2.3 Flow field

To obtain a thorough understanding of the behavior of the aerodynamic drag coefficient, it is essential to conduct a detailed analysis of the flow field. This approach represents a fundamental cornerstone in the field of aerodynamics, a discipline that investigates the behavior of fluids when interacting with solid bodies, as in the case of moving objects studied in this thesis, where velocity plays a central role.

The analysis of the flow field provides a rich source of information about the peculiarities of the flow around the examined object. In the specific context of the aerodynamic drag coefficient, known as  $C_x$ , various factors exert a decisive influence, including the shape of the object, the surface roughness, and, notably, the flow velocity.

The relationship between flow velocity and  $C_x$  is complex and varies depending on the specific shape of the object. In general, it is observed that at lower speeds, the air can flow around the object more smoothly and less turbulently. This can result in a potential decrease in the aerodynamic drag experienced by the object.

Examining the simulations of the front moving belts, noticeable differences can be observed among the analyzed configurations. For the central configuration, there is an area around the tire with a lower flow velocity compared to the other two configurations. Additionally, there is a broader region with medium to high velocities for the internal front configuration, which could explain why a higher

drag coefficient was obtained with this setup.

Clearly, the introduction of the cups has resulted in a reduction of turbulence, explaining the decrease in  $C_x$  values for the two extreme configurations. In this case, the external configuration exhibits a slightly larger area around the tire with lower velocities, indicating lower turbulence and hence a lower  $C_x$ , as confirmed by the observed trend in the  $C_x$  values.

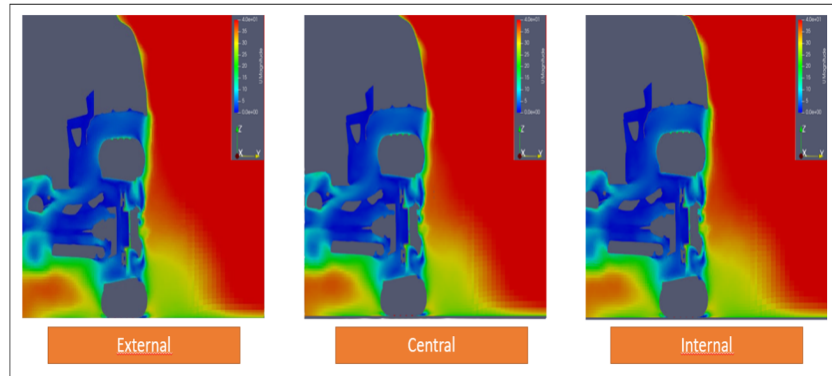


**Figure 6.20:** Flow field - front moving belts

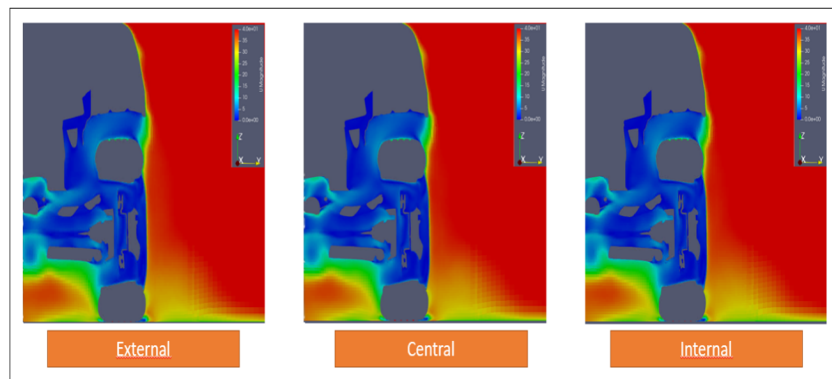


**Figure 6.21:** Flow field - front moving belts with covered tires

The coherence between simulations performed on ParaView and the results obtained through CFD is also confirmed in the case of rear moving belts. An area with medium-low velocities is observed, lower than the central and internal configurations, highlighting the difference between this configuration and the other two.

In this case as well, the introduction of cups has reduced areas with higher turbulence. Although there are slight differences, as previously noted, these discrepancies

tend to offset each other, contributing to maintaining an almost linear coefficient of aerodynamic resistance.

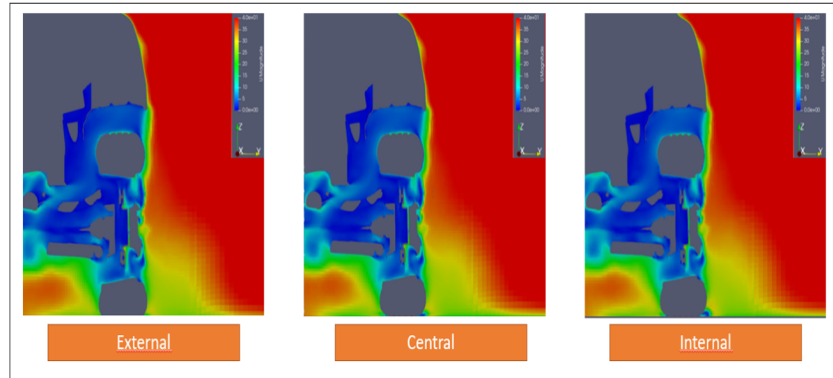


**Figure 6.22:** Flow field - rear moving belts

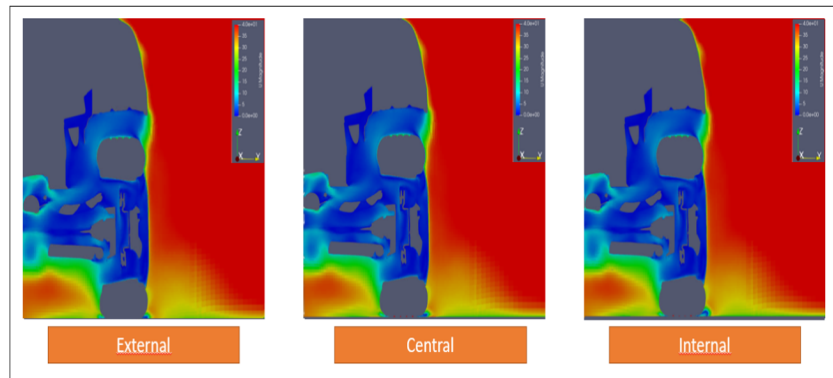


**Figure 6.23:** Flow field - rear moving belts with covered tires

This consistency between simulations using different tools and the evidence obtained through CFD strengthens the validity of the analyses conducted on front and rear moving belts. Observations related to flow areas and turbulence, along with considerations about cup configurations, provide a comprehensive understanding of the aerodynamic interactions at play, contributing to a more in-depth comprehension of the overall system behavior.

## 6.3 Pressure Field

### 6.3.1 Cx correlation

Evident from the images below is the close resemblance between the trends from the CFD simulations and those obtained in the wind tunnel.

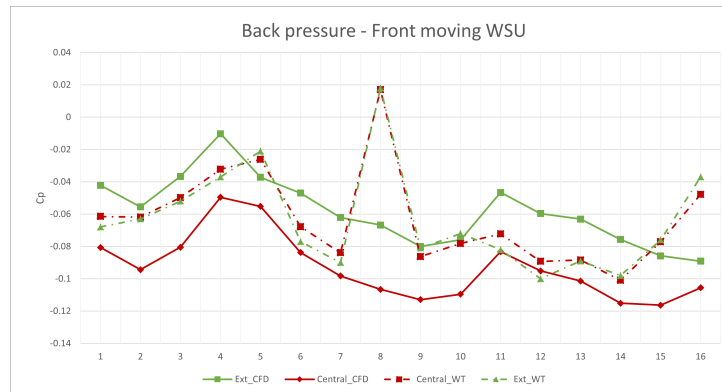


**Figure 6.24:** Comparison of back pressure during front moving belts

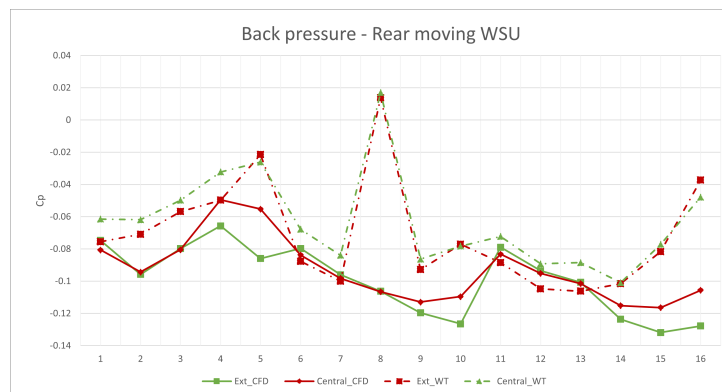


**Figure 6.25:** Comparison of back pressure during rear moving belts

It is noteworthy that there is a peak in the pressure coefficient in the main area slightly to the right of the rear hatch (point 8), which is entirely absent in the CFD. When evaluating a vehicle like the Stelvio in a wind tunnel, several plausible explanations become known, such as local airflow effects. However, the most probable explanation revolves around potential measurement or instrumentation errors: it is possible that an error occurred during the measurement or calibration of the instruments used in the wind tunnel, leading to the recording of anomalous values. Additionally, a significant difference in  $c_p$  is seen between the values

obtained via CFD and those measured in the wind tunnel at point 16. This discrepancy could be attributed to the real-life effect of the deflector, causing a deceleration of the flow and subsequently resulting in an increase in the pressure coefficient.

### 6.3.2 Cz Correlation

The knowledge of the pressure coefficients around the belts, both in the experimental and numerical approach, allows the confirmation that the force acting in that area is the same. As can be seen from the images below, the pressure field trends for the four cases between CFD and WT are remarkably similar to each other. Thus, there is the possibility to confirm that since the results of the CFD simulation for each of the 16 points are close to those in the WT, the simulation could be considered reliable.

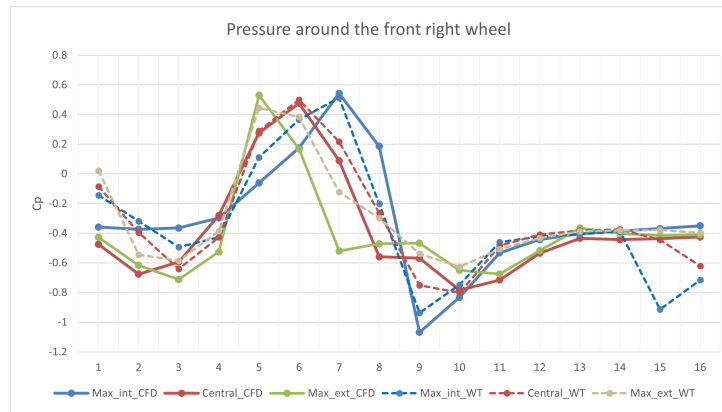


Figure 6.26: Cp comparison - front moving WSU

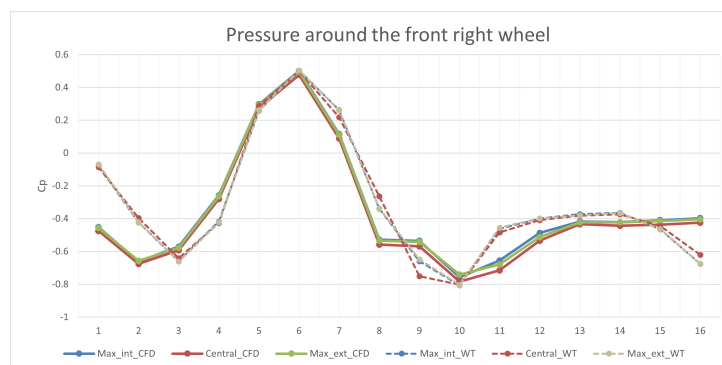
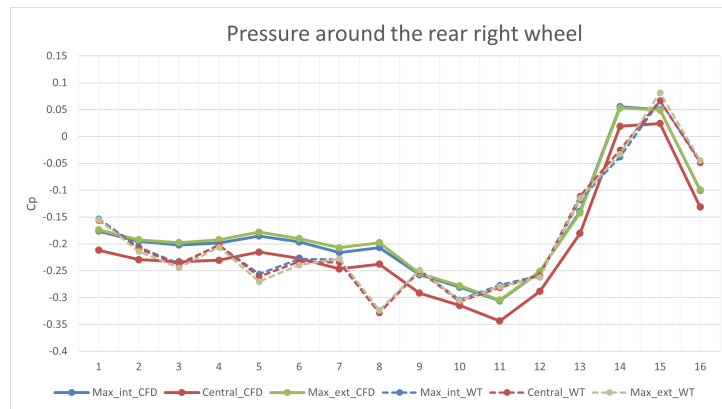
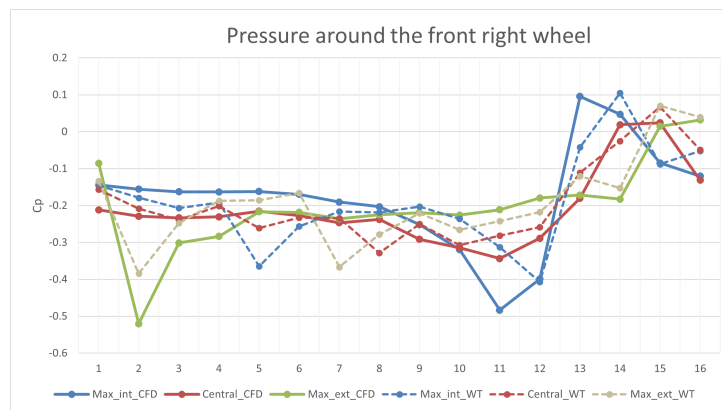


Figure 6.27: Cp comparison - rear moving WSU



**Figure 6.28:** Cp comparison - front moving WSU



**Figure 6.29:** Cp comparison - rear moving WSU

The similarity in the pressure field trends, highlighted by the images, shows an elevated level of agreement between the data obtained through numerical simulation and those measured experimentally. This coincidence strengthens the confidence in the ability of the CFD simulation to accurately be the real flow behavior.

The possibility of confirming the reliability of the CFD simulation based on the similarity of the pressure fields is critically important for the accuracy and validity of the analyses conducted. This allows using the simulation results to draw valid conclusions and make reliable predictions about the behavior of the examined system.

Furthermore, the resemblance between the pressure fields in the CFD simulations and the wind tunnel tests helps show and correct any defects or errors in the

CFD model itself. In the case of significant discrepancies, as seen in many cases in the simulation of the belts positioned in their maximum external configuration, this may suggest the presence of gaps or inconsistencies in the model, which require further consideration and revision in order to improve the accuracy of the simulations and predictive models.

The demonstrated reliability of the computational model, along with its capability to supply accurate predictions about the behavior of the system under investigation, reinforces the confidence in the precise representation of the pertinent physical phenomenon and the provision of valuable insights for analysis and design. This is further evidenced through the following dispersion plots.

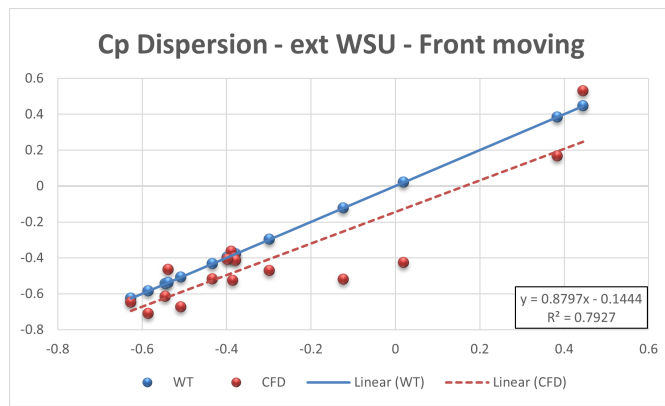


**Figure 6.30:** Cp dispersion ext WSU

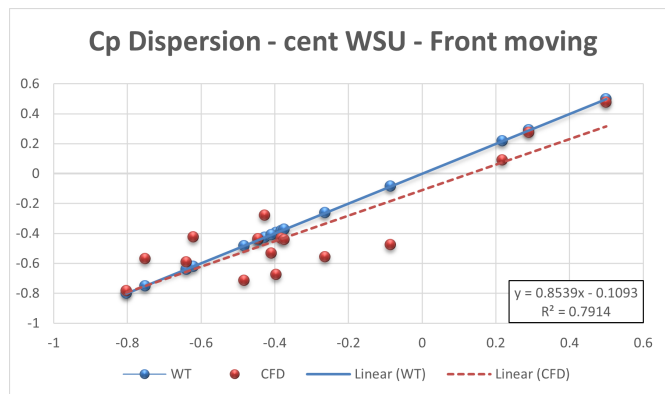


**Figure 6.31:** Cp dispersion cent WSU

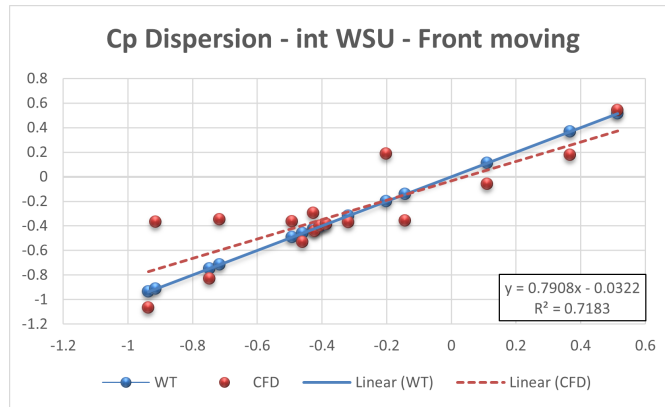


Figure 6.32: Cp dispersion int WSU

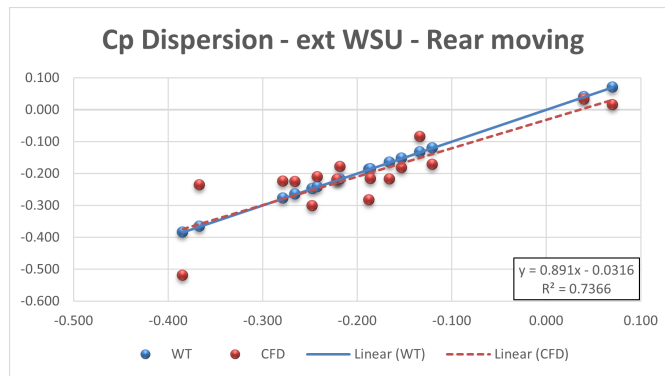


Figure 6.33: Cp dispersion ext WSU

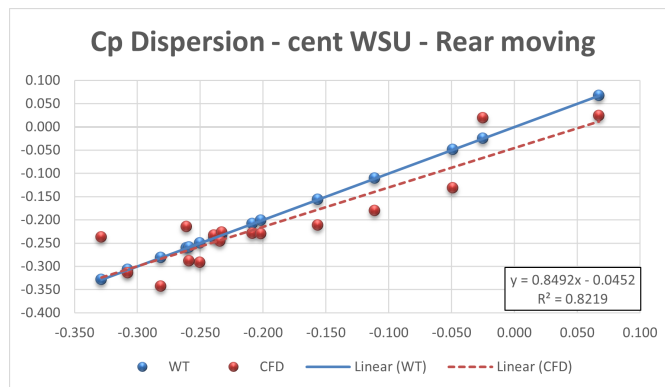
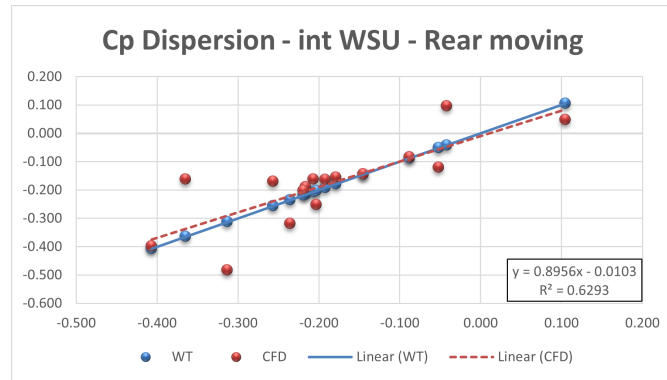


Figure 6.34: Cp dispersion cent WSU



**Figure 6.35:** Cp dispersion int WSU

All cases were graphically represented by initially examining the Front Moving Wind Speed Upstream (WSU) and Rear Moving WSU, both at the front right belt and then at the rear right belt. It was clear that the two trends, or more accurately, the two patterns, were nearly identical, strongly supporting the assertion of a significant correlation between the two methods employed.

The parameter providing this information was the coefficient of determination  $R^2$ . It served as an indicator that, starting from the regression line, summarized in a single value how much the analyzed variable on average deviated from this line. It was equal to 1 when the model perfectly explained the data and equal to 0 if it did not explain them at all. In practice,  $R^2$  values close to 1 indicated a good fit of the model to the data, while values close to 0 suggested that the model was unable to explain the variation in the data significantly.

Both from the graphs and the table of dispersion coefficients, the correctness of the CFD with the replicated tire was confirmed, as well as the correspondence between the experimental and numerical cases.

CONFIGURATIONS	FRONT RIGHT BELT	REAR RIGHT BELT
Front WSU - ext position	0.7927	-
Front WSU - cent position	0.7914	-
Front WSU - int position	0.7183	-
Rear WSU - ext position	-	0.7366
Rear WSU - cent position	-	0.8219
Rear WSU - int position	-	0.6293

**Table 6.2:** Dispersion values

# Chapter 7

## Conclusion

As can be concluded from the analyses conducted in the thesis, there is an observed incongruence, especially in the trends of the aerodynamic drag coefficient, between the results obtained from wind tunnel simulations and CFD. The use of cups in tire simulation emerges as an effective strategy to improve coherence between CFD simulations and tests conducted in wind tunnels.

The observed phenomenon of incongruence between simulations conducted with and without covers may be attributed to several factors, foremost among them being the use of the Moving Reference Frame (MRF). The Moving Reference Frame (MRF) imparts a centripetal velocity component to the volumetric particles within the domain in the Navier-Stokes equations. However, it is crucial to note that despite the influence of the MRF on particle dynamics, it does not effectively induce wheel rotation during the simulation. Instead, the MRF acts as a contribution to the forces involved in particle motion, making adjustments to velocity components and influencing the complexity of the fluid-particle system. The application of the Moving Reference Frame (MRF) does not sufficiently involve the particles in the immediate vicinity of the tire, resulting in a diminished effect. This phenomenon is evident in the observation that the portion of particles situated outside it does not follow the expected or desired movements.

It is also crucial to emphasize the complexity of the airflow around tires. The airflow is characterized by flow separations, vortices, and three-dimensional interactions. Accurately modeling these phenomena requires high spatial and temporal resolution, leading to increased computational costs. The introduction of the covers improves the ability to precisely control the airflow around the tire during simulation helps mitigate undesirable effects stemming from turbulence or irregular flows, thereby contributing to ensuring more correct and reliable results.

Lastly, the adoption of cups results in less external interference during wind tunnel tests or other simulated scenarios. This translates to increased accuracy in reproducing test conditions, further contributing to ensuring consistency between numerical and experimental simulations.

A potential advancement toward greater congruence between CFD simulations and wind tunnel testing involves the introduction of sliding mesh technology. During stationary simulations, particularly with respect to wheel rims, the implementation of a sliding mesh could add realism to the simulations. This technology would enable the movement of the tire mesh, allowing for a more precise and detailed capture of the fluid dynamic effects associated with wheel motion. Such an advancement could contribute to improving the congruence between CFD simulation results and real-world wind tunnel conditions, making numerical analyses more faithful to the physical dynamics of the studied system.

The opportunity to conduct the thesis at Stellantis has proven to be an exceptional experience that provided a comprehensive and in-depth insight into the world of vehicle aerodynamics. Access to both CFD simulations and wind tunnel tests offered an integrated and complementary approach to studying aerodynamic forces on vehicles. The use of Computational Fluid Dynamics allowed for a virtual exploration of the airflow around tires, offering the flexibility to examine a wide range of conditions and configurations. However, it was crucial to balance this approach with wind tunnel tests, providing crucial experimental data to validate and refine numerical models. The integration of both these methodologies has overcome specific challenges related to tire modeling, resulting in a deeper and more accurate understanding of the aerodynamic forces involved. The experience at Stellantis emphasized the importance of collaboration between theory and experimentation, highlighting how the integration of both approaches leads to more reliable and applicable results in the context of vehicle design and optimization.

# Bibliography

- SAE technical paper serie 2002-01-0553, “Computational and experimental evaluation of a pad correction for a wind tunnel balance equipped for rotating wheels” by G. Wickern, E. Base
- SAE technical paper serie 2002-01-0429, “The new 5-belts road simulations system of the IVK winf tunnel design and first results” by J. Wiedemann, J. Potthoff
- Anderson, J. D., Fundamental of Aerodynamics, Second Edition, MxGraw-Hill, Inc. 1991
- P Lesniewicz et al. Aerodynamic analysis of an isolated vehicle eheel. J. Phys.: Conf. Ser. 530 012064, 2014
- T. Lajos T. Regert. Investigation of flow field past rotating wheels of cars. The 12th International Conference on Fluid Flow Technologies, Budapest, Hungary, September 3 – 6 2003